A Study of Sensorless Commutation Methods for Brushless DC Motors

by

Jiahao Kou

A thesis submitted in partial fulfillment of the requirements for the degree of

Master of Science

in

Energy Systems

Department of Electrical and Computer Engineering
University of Alberta

Abstract

Due to advantages including high efficiency, linear speed torque characteristics and better superior speed performance, Brushless DC (BLDC) motors have been applied in many industrial areas, including automotives, aerospace, HVAC, refrigeration, medicine and industrial automation. BLDC motors are controlled in either sensor or sensorless condition, and many control methods have been proposed to improve their performance. This thesis investigates two sensorless control methods based on line voltage differences and the disturbance observer respectively. Each of these two sensorless control methods is first verified through Simulink simulation results, and then implemented in an experimental environment based on the DRV8312 Digital Motor Control Kit from Texas Instruments. To ensure the correct commutation of the BLDC motor, different phase delay compensation algorithms are applied to compensate the time delay from the low pass filters for these two sensorless control methods, respectively. Finally, a comparison is made between these two sensorless drives, and the robustness of the sensorless drives during loading transient is demonstrated by simulation results.

Acknowledgements

I would like to thank my supervisor, Dr. Alan Lynch, for his guidance and support throughout my master program. I would also like to thank the members of my thesis committee, Dr. Qing Zhao and Dr. Yunwei Li, for reviewing my thesis and giving me valuable comments.

I would like to thank my colleagues in the Applied Nonlinear Controls Lab (ANCL): Ning Cao, Hui Xie and Lianfeng Hou for their help in my courses and research works.

My sincere gratitude is dedicated to my parents, my brother, and my girlfriend Hui for their love, support and encouragement during my life at University of Alberta.

Table of Contents

List of Figures

List of Tables

Chapter 1

Introduction

1.1 Background

In [30], it mentions that BLDC motors are better than induction motors and brushed DC motors in many areas. Firstly, BLDC motors are smaller in size, and have higher efficiency because of no losses in the rotor. Secondly, due to the elimination of brushes, BLDC motors have better high speed capability, and they do not need any brush maintenance. Thirdly, BLDC motors have a faster response and a lower radio frequency interference (RFI). Also, BLDC motors are designed with internal shaft position feedback, so that they have higher starting torque compared with AC induction motors. Lastly, compared to induction motors, BLDC motors have much better controllability because of their linear speed torque characteristics.

The world market growth for electric motors in automotive applications is shown in Figure 1.1, derived from the IMS research. As for global issues like fuel shortage and global warming, the market for electric vehicles and hybrid vehicles will continue to increase in the next few decades. With the development of electrically-driven automotive systems, the demand for electric motors is expected to grow, especially for BLDC motor shipments, which are predicted to grow at twice the rate of other motor types.

BLDC motors have been applied in many other areas. For example, in the Heating, ventilation and air conditioning (HVAC) and refrigeration industries, BLDC motors have been applied to reduce the operating power requirements instead of various types of AC motors. For medical applications, BLDC mo-

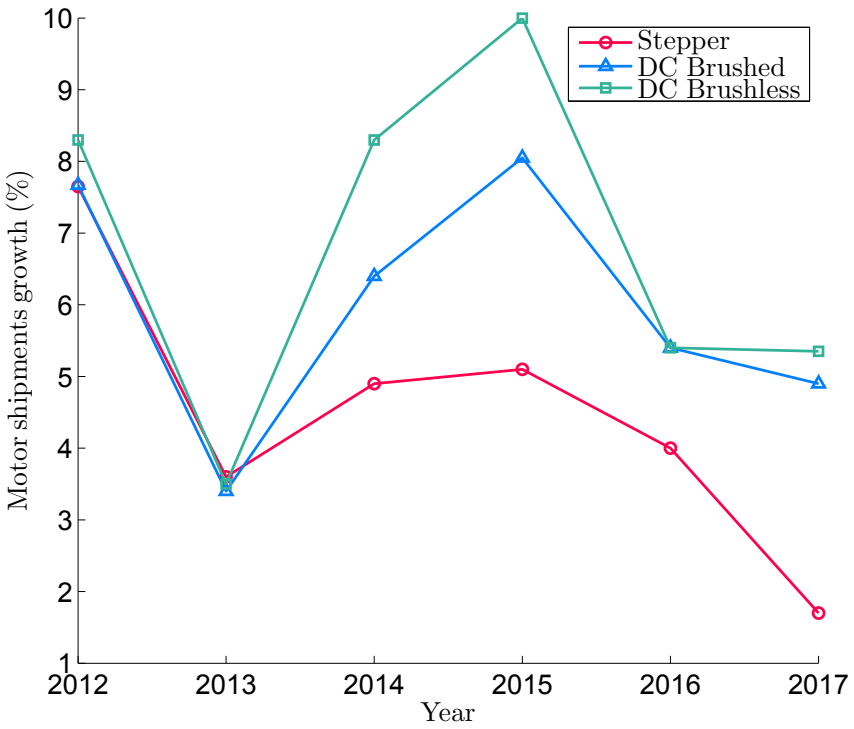

Figure 1.1: World market growth for electric motors in automotive applications

tors, previously not an option, are now surging due to improvements in efficiency and reliability. BLDC motors are also applied to industrial robots and aerospace areas. BLDC motors are taking center stages and will be the future trend, which will drive the growth in the BLDC motor market.

Since BLDC motors play a more and more important role in modern society, it is of great value for us to research on BLDC motor drive systems to make them better for applications in various areas.

1.2 Conventional Control Method Using Hall-effect Sensors

BLDC motors need rotor positions for proper commutation of stator currents. For a permanent magnet AC synchronous (PMAC) motor, a resolver or a shaft encoder is normally applied to detect rotor positions because constant information of rotor positions is required for PMAC motor control [8]. However, for a BLDC motor, one electrical cycle contains only six commutation instants,

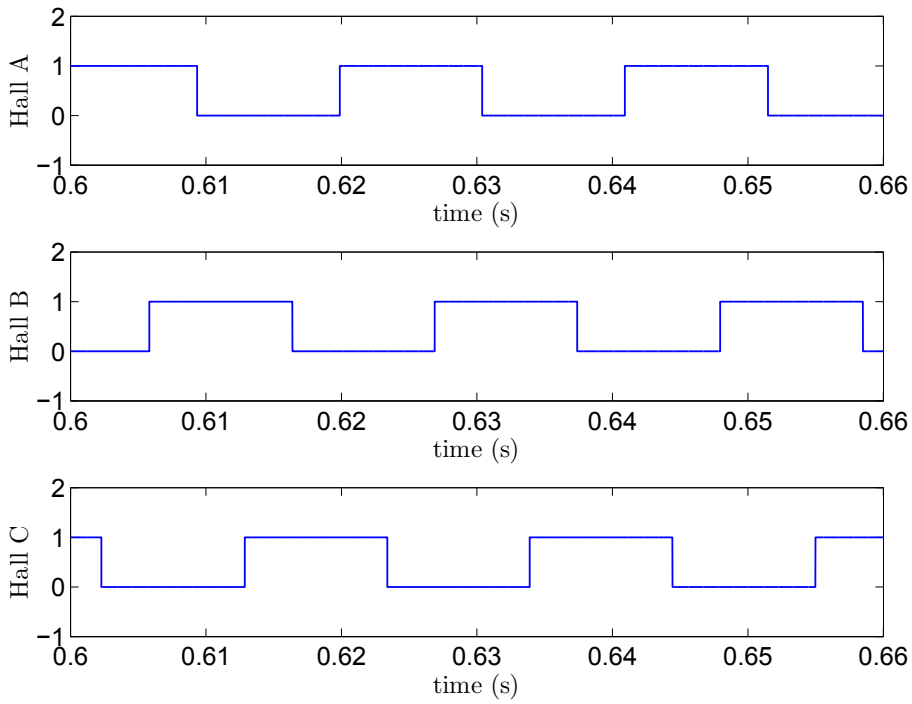

Figure 1.2: Hall-effect sensors outputs at 700 rpm

so Hall-effect sensors are often used, which can reduce the costs [19].

BLDC motors are controlled electronically instead of using mechanical commutation. Hall-effect sensors can be mounted in one of three locations inside the motor to measure the motor's positions. When permanent magnetic north or south poles pass near the Hall-effect sensors, the Hall-effect sensors will generate low or high signals accordingly. Figure 1.2 shows a simulation result of the outputs of Hall-effect sensors at a speed of 700 rpm. Based on the output signals sent from three Hall-effect sensors, the current state can be determined and currents will be applied to corresponding motor coils.

However, the control method based on hall sensors has some drawbacks. High temperature will affect the performance of hall sensors thereby limiting their application areas. The cost and weight of motors will also increase and extra mechanical arrangement need to be mounted [6]. To increase system reliability and reduce system cost, sensorless control of BLDC motors has attracted wide attentions.

1.3 Sensorless Control Methods for BLDC Motors

If a PM motor drive only needs electrical measurements without any requirements for a position sensor, it is called a sensorless drive [2]. There are many kinds of sensorless drives for BLDC motors. Among them, back electromotive force (back-EMF) based methods are the most commonly used category.

Conventional back-EMF based methods utilize the terminal voltage in the floating phase [20][19][13], detection of the conducting state of freewheeling diode in the floating phase [31][6], third harmonic components of back-EMF waveforms [9] and integration of the floating phase back-EMF [1].

However, back-EMFs values are zero at standstill, and it is difficult to detect the zero-crossing points from noises if the motor speed is low, so the low speed performance is limited. For methods based on back-EMFs, a starting procedure is normally required to speed up BLDC motors to a relatively higher speed, and then motors can be controlled by sensorless drives [8].

1.3.1 Terminal Voltage Sensing method

The terminal voltage sensing method is one of the common methods among back-EMFs based sensorless techniques.

For the trapezoidal control of BLDC motors, back-EMFs are required to be in phase with the phase currents, so the motor is able to produce a constant torque [8]. The most commonly way is to detect the zero-crossing points of the back-EMF in the floating phase [22]. There is a 30° offset between zero-crossing points of back-EMFs and current commutation instants, so a 30° phase shift needs to be applied to get the correct commutation instances [20].

Since the back-EMFs are determined with respect to the motor neutral point, the neutral point voltage must be compare with terminal voltages to get the zero-crossing points of back-EMFs. However, neutral points are not available in most BLDC motors. The most commonly used approach is to connect the terminals of the BLDC motor to a Y-connected resistive network. The virtual neutral point voltage can be used to compare with the terminal

voltage in the floating phase to get the zero-crossing points.

However, the virtual neutral point voltage contains lots of electrical noises because the pulse width modulation (PWM) technique is normally applied to drive the inverter. Another approach is to compare terminal voltages with half of the DC link voltage to get back-EMFs zero-crossing points [19]. Work in [28] mentioned that the measurements do not contain any noises if sampling during PWM on time.

Low pass filters are normally applied to attenuate the high frequency harmonics components in terminal voltages introduced by PWM. However, low pass filters will cause a time delay which becomes more obvious when a BLDC motor runs at high speeds range. With no phase compensation, the time delay will restrict the suitable high speed range of BLDC motors. Because the back-EMF magnitude is in proportion to the motor speed, it is unable to detect back-EMFs at standstill and low speed, which is another drawback of terminal voltage sensing method [8]. Therefore, conventional open-loop starting method will be applied to speed up a BLDC motor from standstill.

1.3.2 Freewheeling Diode Conducting State Detection method

Work in [31] proposed an method which can estimate the commutation points on the basis of the conducting state of the freewheeling diode which is in parallel with the power transistor in the floating phase. Six commutation instants for one electrical cycle can be obtained based on whether the freewheeling diode is conducting or not. This detected point leads the next commutation instant by 30 degrees, so a phase shift is required. The conducting condition of the freewheeling diode at the negative side of phase C is derived as:

$$e_c < -\frac{V_1 + V_2}{2} \tag{1.1}$$

where V_1 is the transistors voltage drop, V_2 is the diodes voltage drop and e_c is the back-EMF of phase C. Compared with the back-EMF value, V_1 and V_2 are negligible. When e_c changes from positive to negative, the current flowing through the freewheeling diode at the negative side of phase C will be detected

as.

Because the conducting of the freewheeling diodes relies on back-EMFs value, detection of the rotor position at low speeds is hard to realize, so a starting process is applied [8]. The main drawback of this method is that for detection of current flowing in each freewheeling diode, a separate power supply for the comparator circuit is required [6]. These additional requirements will limit this method in real applications.

1.3.3 Third Harmonic Component Integration method

Works in [29] mentioned that the third harmonic component of back-EMF waveforms are applied to estimate the commutation points. The trapezoidal waveforms of the BLDC motor back-EMFs consist of fundamental and higher order harmonics. After summing the three terminal voltages, the third harmonic component of back-EMF waveforms is obtained [20]:

$$\begin{aligned} V_{result} &= V_{an} + V_{bn} + V_{cn} \\ &= \left(R + L\frac{\mathrm{d}}{\mathrm{d}t}\right)(i_a + i_b + i_c) + e_a + e_b + e_c \\ &= e_a + e_b + e_c \approx 3e_3 sin\,(3\theta_r) \end{aligned} \tag{1.2}$$

where V_{result} is the summation result of the three terminal voltages, V_{an}, V_{bn} and V_{cn} are the phase voltages with respect to the motor neutral voltage, R is the phase stator resistance, L is the phase stator inductance, e_a, e_b and e_c are the phase back-EMFs, i_a, i_b and i_c are the phase currents, e_3 is the third harmonic component of back-EMF waveforms and θ_r is the electrical angle.

Because during each state, the sum of three phase currents $(i_a + i_b + i_c)$ is equal to zero. V_{result} is dominated by the third harmonic component and contains only third-order harmonics (3rd, 6th, 9th). After integrating V_{result}, the third harmonic flux linkage can be obtained as:

$$\lambda = \int V_{result} dt \tag{1.3}$$

where λ is the third harmonic flux linkage [8].

Based on the results in [29], the zero-crossing points of λ are identical to the current commutation points as shown in Figure 1.3. The main advantage

of this technique is that V_{result} does not contain the switching noises caused by PWM signals. In comparison with other sensorless control methods which need a low pass filter, this method requires less filtering [20]. Due to insensitivity to filtering delay, this method can work over a wider speed range. Theoretically, this sensorless commutation method is suitable for a wide speed range and it can work at various load conditions. Its performance at lower speeds is also better because third harmonics can be detected even when the speed is low.

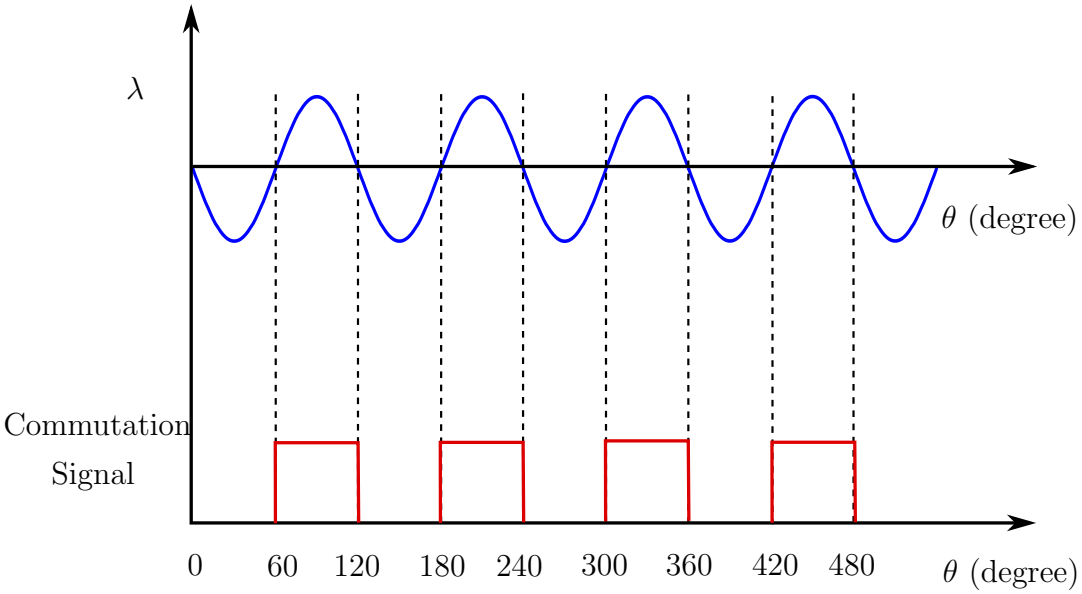

Figure 1.3: Comparison of the zero-crossing points of λ and the commutation signal

1.3.4 Back-EMF Integration Method

Works in [1] proposed another sensorless control method in which the floating phase back-EMF integration result is used to estimate the commutation points. In close proximity to the back-EMFs zero-crossing points, back-EMFs vary approximately linearly with time. The integration process will start if the back-EMF in the floating phase reaches its zero-crossing points. The integration result V_{int} can be derived as:

$$\begin{aligned} V_{int} &= \int_0^t \frac{e(t)}{k} dt \\ &= \frac{mt^2}{2k} \end{aligned} \tag{1.4}$$

where k is the integration gain, t is the integration end time, $e(t)$ is the back-EMF value and m is the slope of the back-EMF waveform.

The integration process will stop when V_{int} reaches the predefined threshold. As the back-EMF magnitude is in proportion to the motor velocity, when the motor speeds up or down, the conduction intervals will decrease or increase due to the fixed predefined threshold voltage as shown in Figure 1.4 [21].

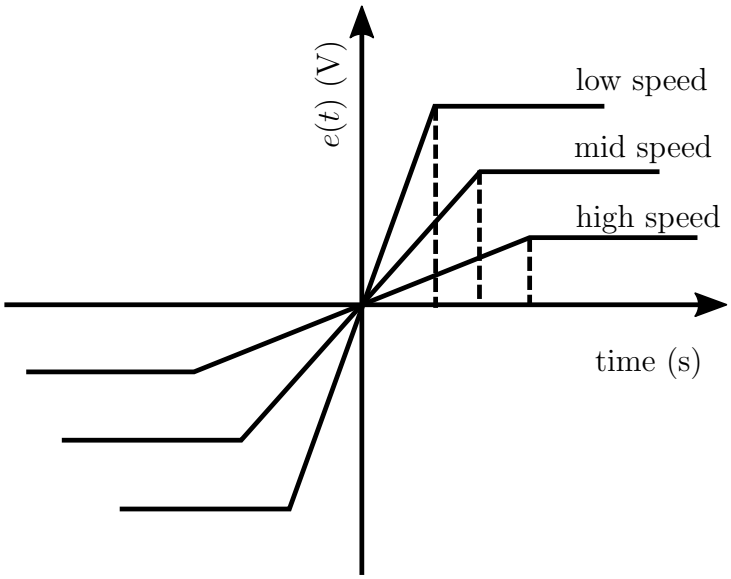

Figure 1.4: Integrated areas of the back-EMF

When V_{int} reaches the predefined threshold, the integration value will be set to zero by a triggered reset signal. To ensure the integration process won't restart before the small current in the floating phase decays to 0, the reset signal should be sustained for a predefined time [8].

However, the back-EMF integration based method has poor performance at low speeds because the integration process will cause errors in estimating the commutation instants when the back-EMF value is small [20].

1.3.5 Optimization

PWM Techniques

Some optimization methods have been proposed. One category is based on PWM techniques. Low pass filters are normally applied in the conventional terminal voltage sensing method to attenuate the high frequency harmonics

components in terminal voltages introduced by PWM. The low pass filter will cause time delay which limits high speed performance, if no phase delay compensation method is applied. However, PWM strategies can eliminate the requirements for low pass filters and work well over a wide speed range [24].

For conventional PWM methods, one upper transistor in one phase and one lower transistor in another phase are conducting at the same time. The remaining phase is the floating phase [31].This approach will increase power losses in the motor side because of the high harmonic components [25].

Work in [36] proposed a direct back-EMF detection method based on the PWM strategy. The direct back-EMF detection method eliminates the need for virtual neutral voltage. In this method, PWM only applies to upper transistors, and lower transistors will be left on. Considering the condition that phase A and B are conducting current, PWM is applied to the upper transistor of phase A and the lower transistor of phase C is on. During PWM off time, the current flowing direction is shown in Figure 1.5 [36]. The terminal voltage of phase C is:

$$V_{cn} = e_c + V_n = \frac{3}{2} e_c \tag{1.5}$$

where V_{cn} is the terminal voltage of phase C, V_n is the neutral voltage and e_c is the back-EMF of phase C.

From the equation above, we can see that V_{cn} is proportional to e_c throughout the PWM off time. The terminal voltage is free of switching noises and is referenced to ground, so the requirement for the motor neutral point voltage is eliminated [8].

Work in [35] proposed an improved method which can detect back-EMFs during PWM on time. For the method mentioned in [36], a minimum PWM off time required to detect back-EMFs, so the maximum duty cycle of this method cannot reach 100% which is desired for some applications in which low battery voltages are applied. To optimize motor operation, back-EMFs are detected during PWM off time when a motor operates in startup and at low-speed conditions. Then back-EMFs are detected during PWM on time when a motor operates in high speed conditions.

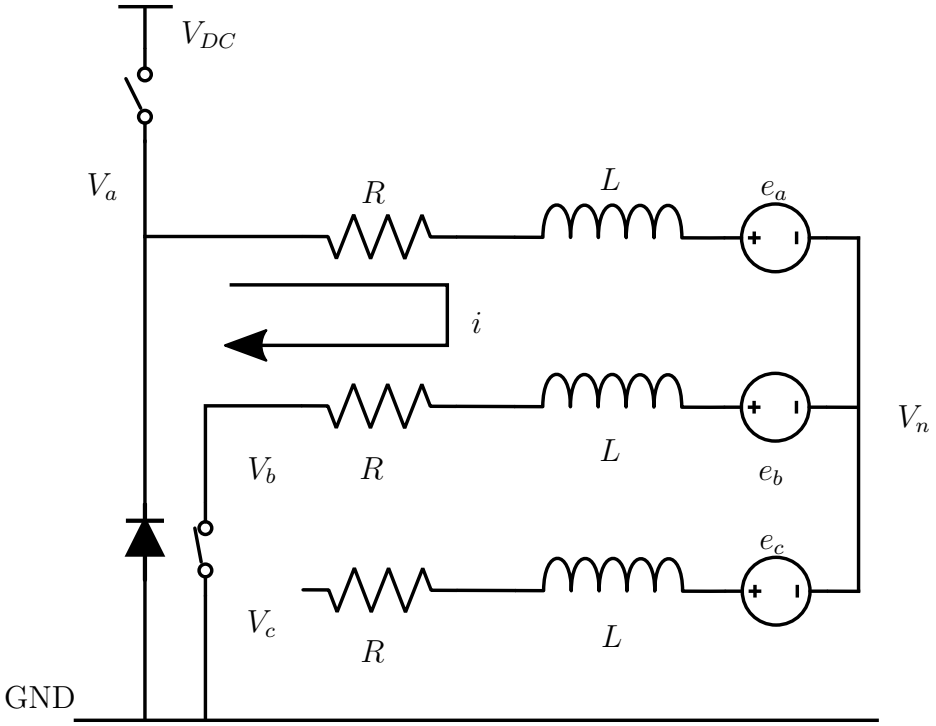

Figure 1.5: Current flowing direction during PWM off time

Lai, Yen-Shin, and Yong-Kai Lin proposed a similar method to detect zero-crossing points of back-EMF waveforms. For PWM on and off states, different methods are applied to detect zero-crossing points, and this sensorless commutation method can work over a wide speed range [24]. The difference between these two methods is that the second one uses a digital controller to calculate zero-crossing points instead of using logical comparisons.

Methods Based on Terminal Line to Line Voltages

Another category is based on terminal line to line voltages rather than using the terminal voltage in the floating phase. In this category, the requirement for the motor neutral voltage can be eliminated.

Based on the work in [4], we can directly get the commutation instants from the average terminal line to line voltages of BLDC motors. The average line to line voltages are in phase with the Hall-effect sensors, so that can be used directly without the need of a phase shift. Also, it does not need the motor neutral voltage compared with the conventional method.

Line voltage differences can also be applied to estimate back-EMF zero-crossing points. Line voltage differences have the same zero-crossing points as the back-EMFs [6]. As line voltages are applied, we can eliminate the requirement for the motor neutral voltage.

The commutation points of BLDC motor currents are identical to the zero-crossing points of line to line back-EMFs, so line to line back-EMFs are applied directly to estimate BLDC motor commutation points without any phase shifts [39]. Work in [26] proposed a novel commutation function based on calculated line to line back-EMFs to estimate commutation instants. Commutation instants occur when the commutation function changes from positive infinity to negative infinity or from negative infinity to positive infinity. Work in [19] proposed a method which uses a circuit constituting a differential amplifier and a comparator to detect zero-crossing points of line to line back-EMFs.

1.3.6 Observer Based Methods

For PMAC motors, observer based methods are often used because they have sinusoidal back-EMFs, and continuous rotor positions information is required [8]. Different observers have also been applied to estimate the rotor positions of BLDC motors.

Observer based methods often take measurements as inputs of the mathematical model of BLDC motors, and take the output as the estimated results. The difference between the measurements and the estimated results is sent back to the mathematical model to make a correction.

The Extended Kalman Filter (EKF) can be employed to estimate rotor positions and motor speed by using average line voltages and the measured phase currents [37]. With the predictive current controller, average line voltages are calculated at the beginning of the sampling interval. However, EKF cannot obtain satisfactory estimation results when the motor speed is low. Based on the work in [11], the computation burdens and difficulties to tuning the control systems are significant drawbacks of EKF based methods, and the sliding mode observer is an attractive method because it is robust despite the measurement noises and parametric uncertainty of the system.

Sliding mode observer is designed based on dynamic equations of BLDC motors to estimate back-EMF values, rotor positions and the motor speed. For conventional methods, a fixed sliding mode observer gain is used to estimate back-EMF values which only suits a particular range of speed. The fixed observer gain will produce multiple zero-crossings when the motor speed is low. Also, it will cause a phase delay in many cases. An improvement has been made to modify the observer gains according to the motor speed, so the estimated back-EMF values are more accurate [7].

Back-EMF differences signals can also be estimated by observers. Work in [22] proposed a new sensorless control method which utilizes an unknown input observer. The unknown input observer is independent of the rotor speed and can be used to estimate back-EMF differences. As shown in table 1.1, the estimated back-EMF differences are used in the commutation functions to get commutation instants.

Electrical Degree	Commutation Function
0-60°	$\hat{e}_{bc}/\hat{e}_{ca}$
60°-120°	$\hat{e}_{ab}/\hat{e}_{bc}$
120°-180°	$\hat{e}_{ca}/\hat{e}_{ab}$
180°-240°	$\hat{e}_{bc}/\hat{e}_{ca}$
240°-300°	$\hat{e}_{ab}/\hat{e}_{bc}$
300°-360°	$\hat{e}_{ca}/\hat{e}_{ab}$

Table 1.1: Commutation function for the unknown input observer

For methods above, continuous rotor positions information is estimated. However, for trapezoidal control of BLDC motors, only 6 commutation points are needed for one electrical cycle, so the complex observer based methods above are not necessary for the control of BLDC motors. Disturbance observer structure can be used to estimate the back-EMF differences signals [39]. This method is easier to implement, and it can precisely estimate the six commutation instants.

1.4 Summary of Contributions

This thesis implements and verifies two sensorless control methods based on line voltage differences and the disturbance observer respectively. Instead of sampling terminal voltages during PWM on time to avoid noises [6], this thesis uses a simpler method in which low pass filters are applied to filter out the high frequency harmonics components introduced by PWM. Compensation methods are included in the sensorless drives to compensate the phase delay introduced by the low pass filters, which will guarantee the high speeds operation of the BLDC motors. Also, the robustness of the sensorless control methods during loading transient is demonstrated by simulation results.

1.5 Thesis Outline

Chapter 2 makes a detailed analysis of the fundamentals of BLDC motors. Firstly, it provides an introduction to the BLDC motor structure with emphasis on the stator and rotor. Chapter 2 also presents the equivalent circuit and the mathematical model of a BLDC motor, which are applied in the derivations of Chapter 4 and Chapter 5. Back-EMF, which is the basis of the sensorless control methods applied in this thesis, is analyzed. Finally, a comparison is made between BLDC motors and PMSMs with respect to power density, power losses, control complexity, and torque ripples.

Chapter 3 outlines the experimental environment of this thesis. The DRV8312 Digital Motor Control Kit, in essence a Piccolo F28035 controlCARD, a DRV8312 Digital Motor Control board and a BLDC motor, on which all the experiment work is based, is introduced and discussed.

Chapter 4 presents a six-step sensorless control method based on the line voltage differences. The Simulink simulation results verify that the line voltage differences have the same zero-crossing points as the back-EMFs. In order to get the six commutation instants for one electrical cycle of the BLDC motor, a phase delay compensation method is applied in consideration of the time delay caused by low pass filters. This sensorless drive is implemented in the

experimental environment under different speed conditions.

Chapter 5 introduces another six-step sensorless control method based on the disturbance observer. The disturbance observer is applied to estimate back-EMF differences. The Simulink simulation results show that the zero-crossing points of the back-EMF differences are identical to the BLDC motor commutation instants. A different phase delay compensation method is applied to compensate for the time delay caused by the disturbance observer structure. The sensorless control method is further verified in the experimental environment. Finally, we make a comparison of these two sensorless drives.

Chapter 6 summarizes the thesis and makes discussions on possible future research directions.

Chapter 2

Fundamentals of the BLDC Motor

2.1 Introduction

In this chapter, we will make an introduction to the fundamentals of the BLDC motor mainly based on the theories in these three references [10][23][40]. Based on the back-EMF waveform shapes, (i.e., sinusoidal and trapezoidal), the permanent magnet synchronous machines can be classified into two different types. The trapezoidal type is called the BLDC motor and the sinusoidal type named the PMSM.

Figure 2.1 [23] shows waveforms of BLDC motors. For one electrical cycle of a BLDC motor, it contains six states. During each state, two phases are conducting and each phase will be excited for 120°. The induced back-EMFs are in the trapezoidal shape, and the constant magnitude remains for 120°. During the change states (from maximum to minimum, or from minimum to maximum), the induced back-EMFs vary linearly.

2.2 BLDC Motor Structure

Figure 2.2 [12] shows the fundamental structure of a BLDC motor. A BLDC motor contains a rotating part, called the rotor, and a stationary frame, called the stator. In this example, the rotor has two pairs of north and south permanent magnet poles. The stator acts as the armature because it will be energized, and the stator current will generate the rotating magnetic field. As

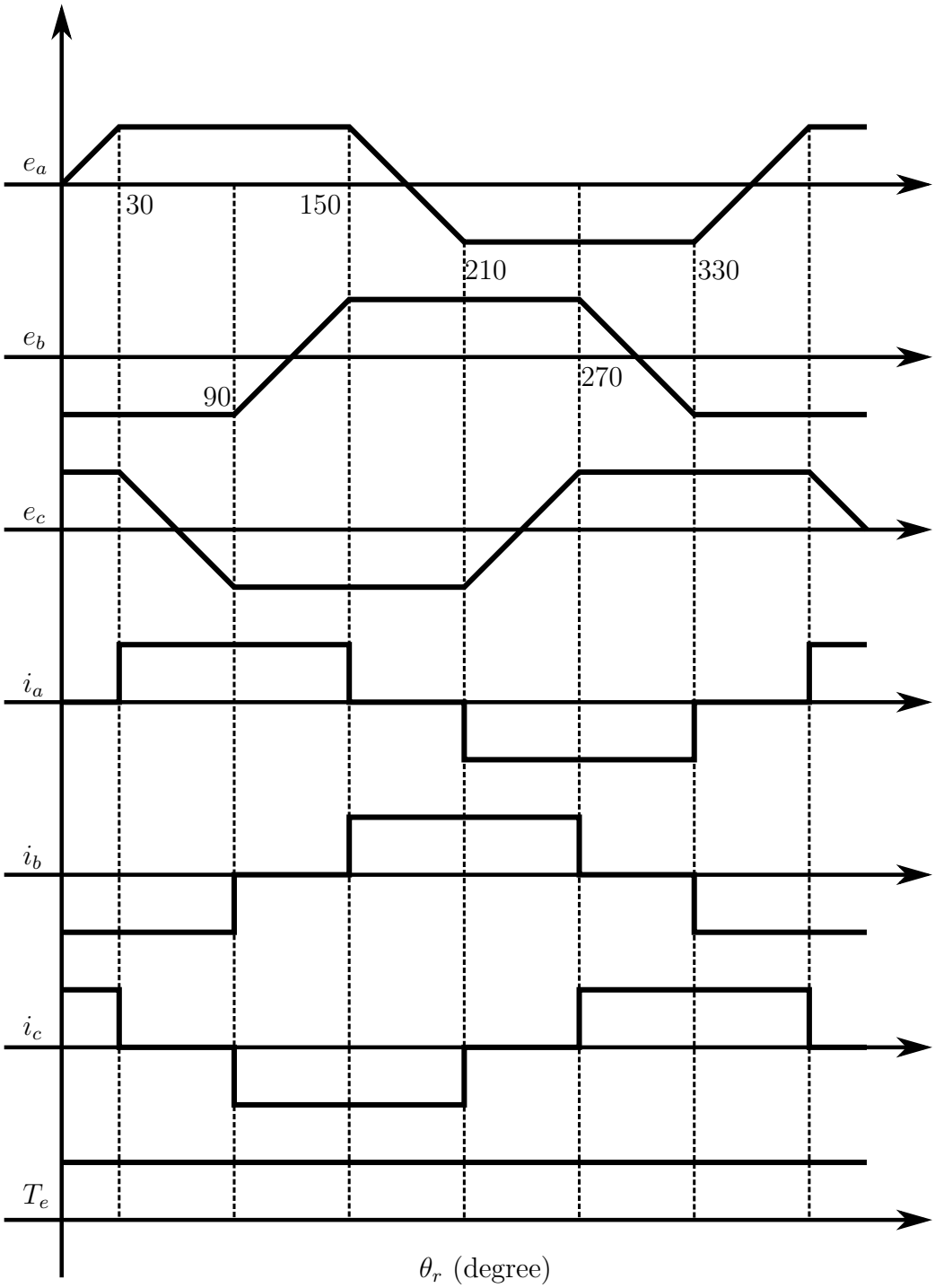

Figure 2.1: Brushless DC motor waveforms

mentioned above, BLDC motors are synchronous machines, which means that the stator and the rotor generate magnetic fields of the same frequency [40].

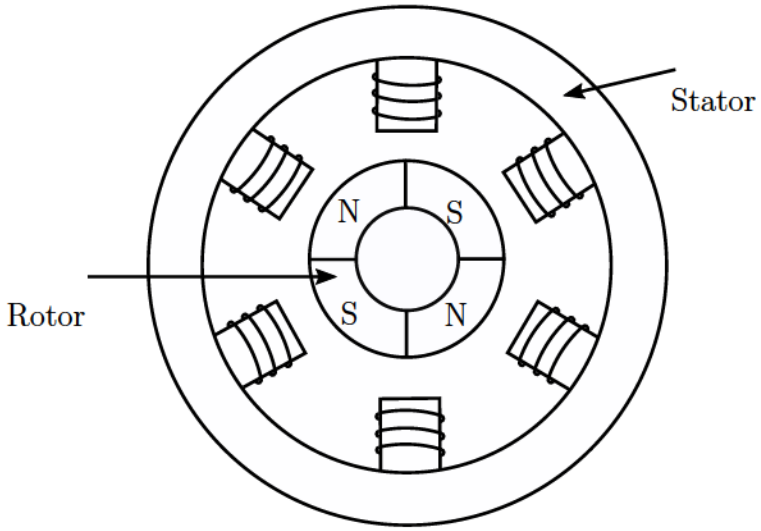

Figure 2.2: Fundamental BLDC motor structure

As mentioned in [27], the windings distribution is different from that of an induction motor. To increase efficiency and torque, BLDC motors normally use star connected stator windings. For each winding, it consists of numerous of coils, which are interconnected with each other. The stator can be slotted or slotless. The slotless stator has a lower inductance, so the BLDC motor is able to run at higher speeds.

Permanent magnets typically form the rotor of a BLDC motor. Different BLDC motors may have various number of pole pairs. Increasing the number of pole pairs will increase the motor torque, but this will limit the maximum possible speed [14].

The material used for the construction of permanent magnets will also affect the maximum torque of BLDC motors as described in [40]. Traditionally, Ferrite magnets are the material used for permanent magnets because of their low price. Ferrite magnets have low flux density for a given volume, and this disadvantage will limit the maximum torque. Nowadays, rare earth alloy magnets (e.g., Samarium Cobalt, Neodymium and the alloy of Neodymium, Ferrite and Boron) are becoming more popular because of their higher magnetic density, and motors using these alloy magnets have a smaller size when

comparing with motors of same weight using ferrite magnets.

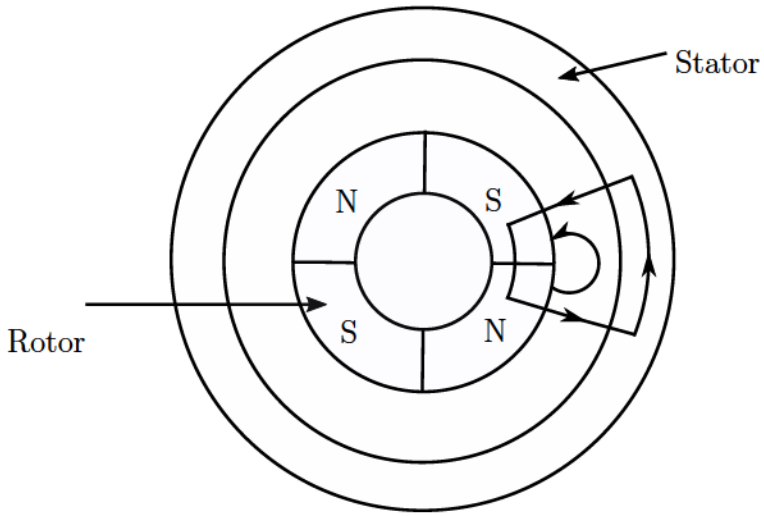

Figure 2.3: A BLDC motor with the flux paths

2.3 Magnetic Circuit Model

This section makes an introduction to the magnetic circuit model of the BLDC motor based on the reference [10]. Figure 2.3 [10] shows two types of flux paths. One magnet flux starts from the north pole, and then it crosses the air gap. When the magnet flux reaches the stator, it will be separated into two parts. Then each of the separated magnet flux will cross the air gap again and travel towards the adjacent two south poles.

In addition to the magnet flux path mentioned above, some magnet flux will not cross the air gap to the stator, and it will directly travel towards the adjacent magnet pole instead as shown in Figure 2.3 [10]. This kind of flux is called the magnet leakage flux.

We can model one adjacent pole pair as shown in Figure 2.4 [10]. The magnet poles is represented by a flux source ϕ_r with its magnet reluctance R_m. The modeling parameters are shown in Table 2.1.

The leakage flux ϕ_l is very small which can be ignored. R_r and R_s are small when comparing with R_g. R_r and R_s can be treated as a small part of

Name	Description	Name	Description
ϕ_r	flux source	R_m	flux source reluctance
R_g	air gap reluctance	R_l	leakage reluctance
R_r	rotor steel reluctance	R_s	stator steel reluctance
ϕ_g	air gap flux	ϕ_l	leakage flux
ϕ	magnet flux		

Table 2.1: Magnetic circuit model parameters

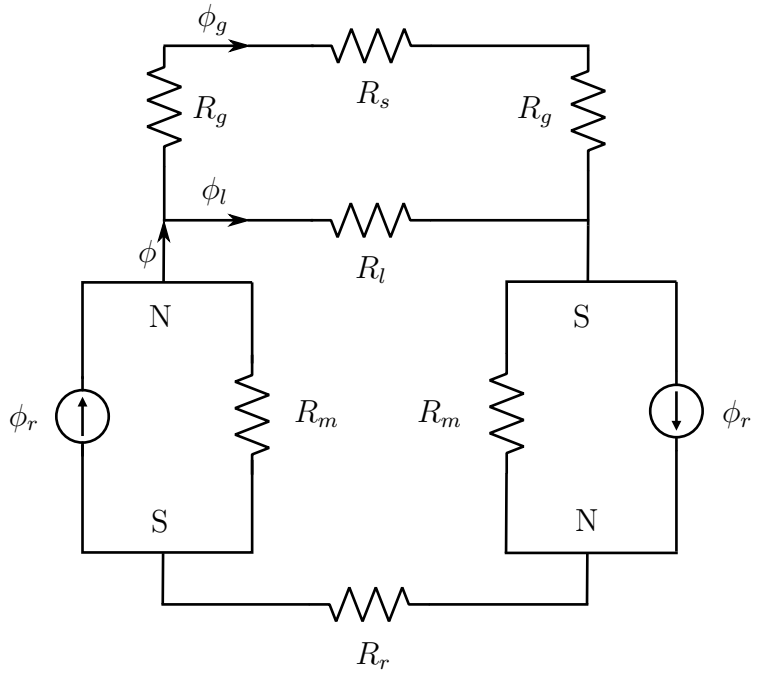

Figure 2.4: A magnetic circuit for BLDC motor

R_g. The equivalent reluctance $(R_r + R_s + 2R_g)$ can be simplified as:

$$R_r + R_s + 2R_g = 2K_r R_g$$

where K_r is the reluctance factor and it is slightly bigger than one.

By determining Norton equivalent circuit, the magnetic circuit can be simplified into Figure 2.5 [10].

The mutual flux between one pole pair and a stator coil can be showed in Figure 2.6 [10]. The total flux ϕ linking the coil comes from two sources: ϕ_1 is the flux from the coil current and ϕ_m is the flux from the permanent magnet.

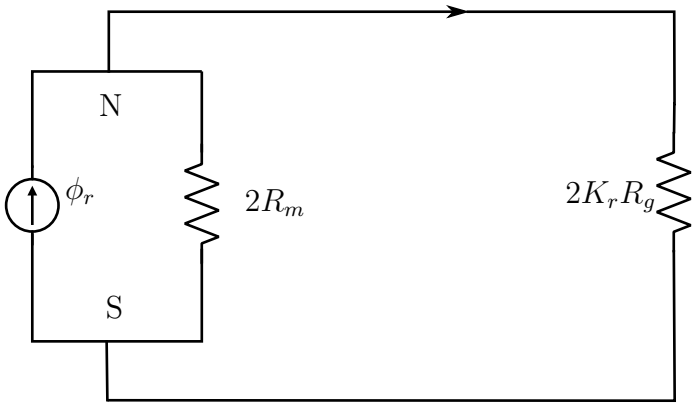

Figure 2.5: Simplification of the magnetic circuit

These fluxes can be expressed as following:

$$\phi = \phi_1 + \phi_m$$

$$\phi_1 = \frac{Ni}{R + R_m}$$

$$\phi_m = \frac{R_m \phi_r}{R + R_m}$$

where R is the reluctance seen from the stator coil, N is the winding turns, i is the current flowing in the winding.

The flux linkage λ is:

$$\lambda = Li + N\phi_m$$

where L is the self inductance.

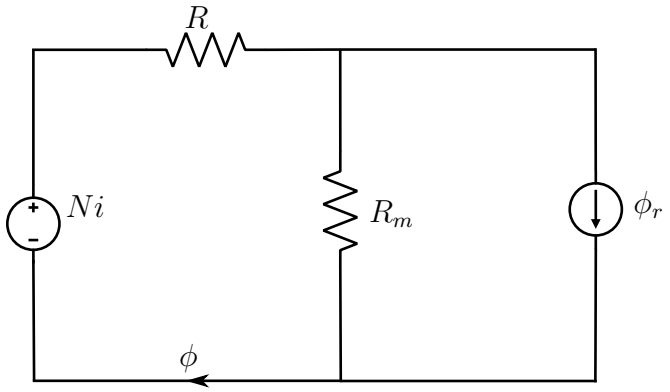

Figure 2.6: Magnetic circuit considering the mutual coupling

2.4 Modeling of a BLDC Motor

The BLDC motor modeling is based on the reference [23]. For the three stator windings of a BLDC motor, the electrical relationships can be represented with the equation below:

$$\begin{bmatrix} V_{an} \\ V_{bn} \\ V_{cn} \end{bmatrix} = \begin{bmatrix} R & 0 & 0 \\ 0 & R & 0 \\ 0 & 0 & R \end{bmatrix} \begin{bmatrix} i_a \\ i_b \\ i_c \end{bmatrix} + \frac{\mathrm{d}}{\mathrm{d}t} \begin{bmatrix} L_{aa} & L_{ab} & L_{ac} \\ L_{ba} & L_{bb} & L_{bc} \\ L_{ca} & L_{cb} & L_{cc} \end{bmatrix} \begin{bmatrix} i_a \\ i_b \\ i_c \end{bmatrix} + \begin{bmatrix} e_a \\ e_b \\ e_c \end{bmatrix} \tag{2.1}$$

where V_{an}, V_{bn} and V_{cn} are the phase voltages referenced to the motor neutral voltage, i_a, i_b and i_c are the phase currents, e_a, e_b and e_c are the phase back-EMFs, R is the phase stator resistance which is same for three phases, L_{aa}, L_{bb} and L_{cc} are the self-inductances, L_{ab}, L_{ba}, L_{ac}, L_{ca}, L_{bc} and L_{cb} are the mutual inductances.

If three phases are symmetric and the rotor reluctance is identical with the change of electrical angle, the three self-inductances are same and the six mutual inductances are equal to each other as:

$$L_{aa} = L_{bb} = L_{cc} = L_s \tag{2.2}$$

$$L_{ab} = L_{ba} = L_{ac} = L_{ca} = L_{bc} = L_{cb} = M \tag{2.3}$$

The equivalent inductance L can be calculated as:

$$L = L_s - M \tag{2.4}$$

Assuming that the phase currents are symmetric, that is

$$i_a + i_b + i_c = 0 \tag{2.5}$$

Then the electrical relationships can be simplified and the BLDC motor can be modeled as:

$$\begin{bmatrix} V_{an} \\ V_{bn} \\ V_{cn} \end{bmatrix} = R \begin{bmatrix} 1 & 0 & 0 \\ 0 & 1 & 0 \\ 0 & 0 & 1 \end{bmatrix} \begin{bmatrix} i_a \\ i_b \\ i_c \end{bmatrix} + \frac{\mathrm{d}}{\mathrm{d}t} \begin{bmatrix} L & 0 & 0 \\ 0 & L & 0 \\ 0 & 0 & L \end{bmatrix} \begin{bmatrix} i_a \\ i_b \\ i_c \end{bmatrix} + \begin{bmatrix} e_a \\ e_b \\ e_c \end{bmatrix} \tag{2.6}$$

2.5 Equivalent Circuit for a BLDC Motor

For a three-phase BLDC motor, the electrical circuit model can be shown in Figure 2.7. In this circuit, R represents the resistance component of the stator winding and L represents the inductive component of the stator phase winding.

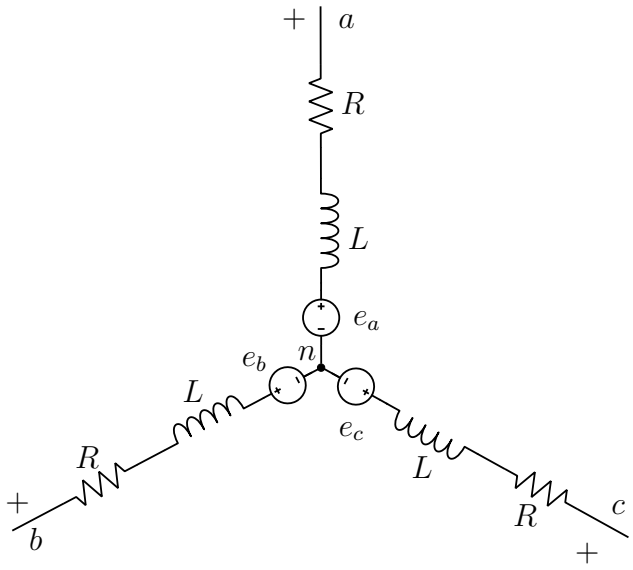

Figure 2.7: Equivalent circuit for BLDC motor

e_a, e_b and e_c are the phase back-EMFs. Because the resistance and inductance are very small for the BLDC motor, the phase currents need to be limited during starting up. Normally, PWM technique is applied for BLDC motor control, and a small duty cycle is set during starting up.

2.6 Back-EMF

This section introduces the back-EMF of a BLDC motor based on the reference [23]. When starting the BLDC motor, stator coils will be energized and a torque will be generated on the rotor. Then the rotor will begin to rotate and the flux linkage in the stator coils will vary depending on permanent magnets locations. According to Faraday's law of induction, a voltage will be induced across the stator windings due to the varying flux linkage. This induced voltage is referenced to back-EMF. The polarity of voltage induced is

governed by Lenz's law. That is, the back-EMF will always try to keep the flux linkage from changing its present value.

For BLDC motors, the back-EMFs are in trapezoidal shape. The peak value of the back-EMFs is E_p which can be calculated as:

$$E_p = K_e \omega \tag{2.7}$$

where ω is the mechanical speed of the motor in rad/s, K_e is back-EMF constant and its unit is V/(rad/s).

K_e can be calculated as:

$$K_e = NBlr \tag{2.8}$$

where B is the flux density, N represents the conductors number per phase, l is the conductor length, r is the air gap radius between the motor rotor and stator.

From the equations above, the peak value of the back-EMFs depends mainly on ω, B and N. Once the motor is designed, the back-EMF constant K_e remains the same. The peak value of the back-EMFs is proportional to the mechanical speed of the rotor.

The instantaneous back-EMFs can be written as:

$$e_a = f_a(\theta_r) K_e \omega \tag{2.9}$$

$$e_b = f_b(\theta_r) K_e \omega \tag{2.10}$$

$$e_c = f_c(\theta_r) K_e \omega \tag{2.11}$$

where θ_r is the electrical degree, f_a, f_b and f_c are in the trapezoidal shape as the back-EMFs, and their peak magnitude is 1.

2.7 Electromagnetic Torque

From the energy conversion point, a BLDC motor converts electrical power to mechanical power to make the motor rotate. Each phase of a BLDC motor is composed of a resistive component and an inductive component [23].

The stator current flowing through the winding will create ohmic losses or heat in the winding resistor. The current will also create a magnetic field

that stores energy. When phase currents flow through back-EMF sources, the instantaneous power $P_{instant}$ absorbed by sources can be derived as:

$$P_{instant} = e_a i_a + e_b i_b + e_c i_c \tag{2.12}$$

To satisfy the conservation of energy, this power will be converted to mechanical power $T_e\omega$. The electromagnetic torque is given by:

$$T_e = \left[e_a i_a + e_b i_b + e_c i_c\right] \frac{1}{\omega} \tag{2.13}$$

Because back-EMFs are proportional to speed, the electromagnetic torque can be derived as [23]:

$$\begin{aligned} T_e &= K_t \left[f_a\left(\theta_r\right) i_a + f_b\left(\theta_r\right) i_b + f_c\left(\theta_r\right) i_c\right] \\ &= K_t(2I_{pd}) \end{aligned} \tag{2.14}$$

where I_{pd} is the peak value of the phase current, K_t is the torque constant and its units are Nm/A. Once the motor is designed, K_t is a constant. As a result, the electromagnetic torque is directly proportional to the stator currents of a BLDC motor.

K_e and K_t are numerically equal. The units for back-EMF constant K_e and the torque constant K_t are equivalent if they are all in SI units as shown in the equation below:

$$\text{Nm/A} = \text{V/(rad/s)} = \text{kg} \cdot \text{m}^2/\text{A} \cdot \text{s}^2 \tag{2.15}$$

2.8 Electromechanical Model

For BLDC motors, the absorbed instantaneous power of back-EMF sources will be converted to mechanical power $T_e\omega$.

The electromagnetic torque is used to drive the motor rotor to rotate. Assuming that the system inertia is J, friction coefficient is B, and the load torque is T_1 if the BLDC motor drives a load, the equation for the electromechanical model of the BLDC motor can be shown as [23]:

$$J\frac{d\omega}{dt} + B\omega = (T_e - T_1) \tag{2.16}$$

and the relationship between the motor synchronous speed and the rotor position can be expressed as:

$$\frac{d\theta_r}{dt} = \frac{p}{2}\omega \tag{2.17}$$

where p is the rotor poles number, ω is the mechanical speed of the motor in rad/s, θ_r is the rotor position in rad.

At the moment a BLDC motor starts, there is no back-EMF, and the stator current will produce maximum electromagnetic torque on the motor rotor. The motor will speed up, and the peak values of back-EMFs will also increase proportionally. During this process, the stator currents will decrease, and the motor speed will become stable finally.

2.9 Comparisons between BLDC Motors and PMSMs

In this section, some comparisons will be made between BLDC motors and PMSMs on their output power and torque ripples based on the reference [23]. The rms values of the stator currents are:

$$I_m = \frac{I_{pm}}{\sqrt{2}} \tag{2.18}$$

$$I_d = \sqrt{\frac{2}{3}} I_{pd} \tag{2.19}$$

where I_{pm} and I_{pd} are the peak values of the stator currents in PMSMs and BLDC motors, respectively. I_m is the rms value of the stator current in PMSMs, and I_d is the rms value of the stator current in BLDC motors.

From the equations above, we can see that BLDC motors have a smaller rms value than that of the sinusoidal PMSMs if their stator currents have the same peak value. Assuming that PMSMs and BLDC motors have the same ohmic losses, the relationship can be derived as:

$$3I_m^2 R = 3I_d^2 R \tag{2.20}$$

where R is the phase stator resistance which is the same for all three phases.

Based on the analysis above, the relationship between the peak value of PMSMs and BLDC motors currents can be derived as:

$$I_{pd} = \frac{\sqrt{3}}{2} I_{pm} \tag{2.21}$$

From the current waveforms of a BLDC motor, we can see that only two of the three phases are conducting at the same time. Consequently, the output power of a BLDC motor is contributed by only two phases. For a PMSM, all three phases have currents and contribute to output power. Assuming that PMSMs and BLDC motors back-EMFs have the same peak value E_p, the ratio of a BLDC motor and a PMSM output power can be calculated as:

$$\text{Power output radio} = \frac{\text{BLDC motor power}}{\text{PMSM motor power}} \tag{2.22}$$

$$= \frac{2 \times E_p \times I_{pd}}{3 \times \frac{E_p}{\sqrt{2}} \times \frac{I_{pm}}{\sqrt{2}}} = 1.1547 \tag{2.23}$$

Based on the analysis above, If PMSMs and BLDC motors have same ohmic losses, the output power of BLDC motors will be 15.4 % higher than that of PMSMs. For BLDC motors, only two phases are conducting currents at the same time, so the duty cycle of the phase currents is smaller than that of PMSMs. The power losses are smaller in BLDC motors, and the inverter thermal reliability is also better. Although, the currents of BLDC motors and PMSMs both have variable frequencies, the rectangular phase currents of BLDC motors have lower control complexity compared with PMSMs.

The torque ripples of BLDC motors are higher than PMSMs. During the finite current transition time, torque ripples are created at each commutation point. Torque ripples will be created whenever currents or back-EMF waveforms are not ideal. For low-performance applications, the torque ripples are rarely significant. However, torque ripples are hard to eliminate and this will limit the use of BLDC motors in applications where minimum torque ripples are required. Knowing how to minimize torque ripples is very important for high-performance applications.

2.10 Summary

In this chapter, we make an introduction to the BLDC motor structure, the magnetic circuit model and the electrical model of a BLDC motor. Back-EMF and electromagnetic toque concepts are also introduced. Finally a comparison is made between PMSMs and BLDC motors. BLDC motors have a higher output power but with larger torque ripples.

Chapter 3

Experimental Environment

In this thesis, all the experiment work is based on the DRV8312-C2 kit, which is developed by Texas Instruments. This kit is a Medium Voltage Digital Motor Control (DMC) kit. In this chapter, an introduction will be made to the hardware details and the development environment.

3.1 Hardware Overview

The DRV8312 Digital Motor Control Kit includes a Piccolo F28035 controlCARD, a DRV8312 Digital Motor Control (DMC) board, a BLDC motor and a 24 V AC/DC supply with 2.5 A of current.

Figure 3.1 shows the diagram of the Kit. Figure 3.2 shows the picture of DRV8312 DMC board, which has a socket for the Piccolo F28035 controlCARD with a built-in isolated XDS100 emulator. The Piccolo F28035 controlCARD acts as the control block and the DRV8312 DMC board is the motor driver.

Based on the Texas Instruments' document [3], debuggers are useful tools to debug software applications on hardware platforms, because the debuggers are able to access the processors and the registers on hardware platforms. On the F28035 controlCARD, the F28035 C2000 controller works with the XDS100 emulation hardware. The emulator is applied to communicate with the F28035 C2000 controller, which is the target processor, and the debugger is the user interface to the communication information. A USB cable is applied to connect the debugger and the laboratory computer. Joint Test Action Group (JTAG) is the emulation logic protocol for the F28035 C2000 controller.

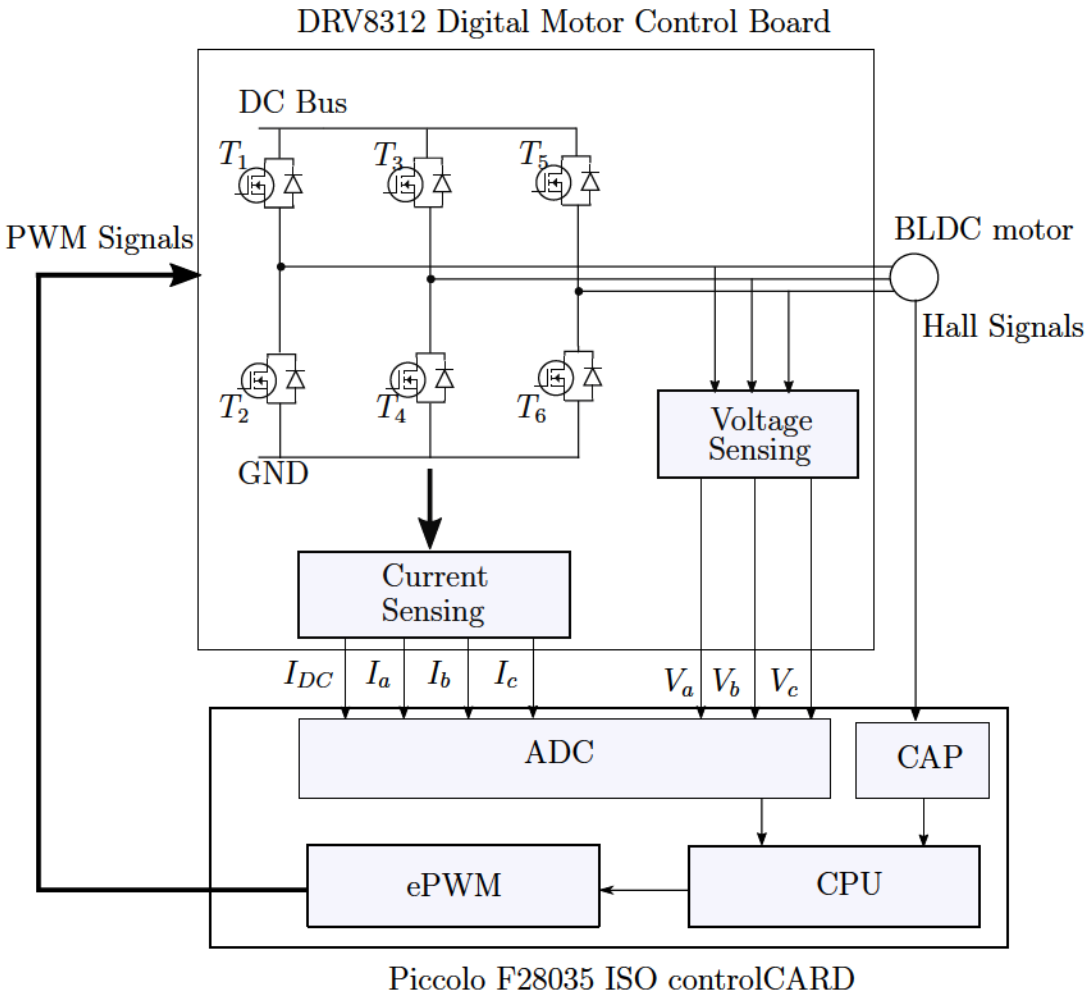

Figure 3.1: Diagram of the DRV8312 Digital Motor Control Kit

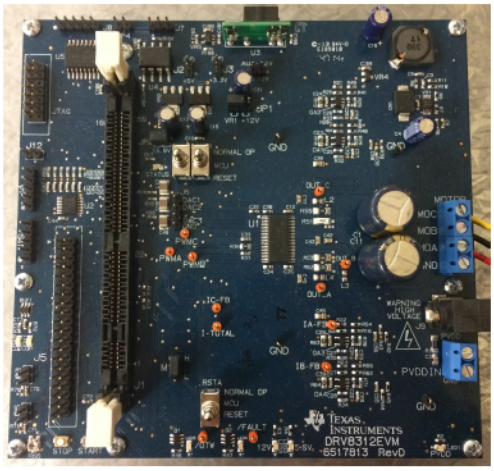

Figure 3.2: DRV8312 Digital Motor Control (DMC) board

3.2 Piccolo F28035 ISO controlCARD

The Piccolo F28035 ISO controlCARD is the evaluation board for the F28035 C2000 controller. As shown in Figure 3.1, this controlCARD includes the key peripherals like Analog-to-Digital converter (ADC), Enhanced pulse width modulator (ePWM), CAP and GPIOs. The CAP peripheral is applied to read the Hall-effect sensor signals. These peripherals signals communication is via the controlCARD pins. Figure 3.3 shows the picture of Piccolo F28035 ISO controlCARD.

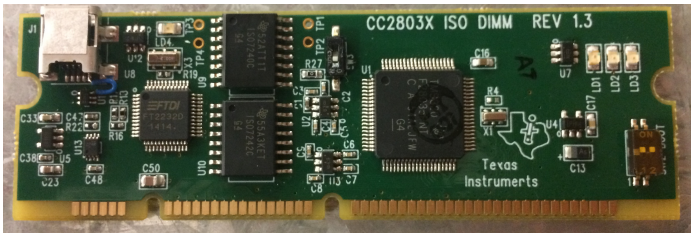

Figure 3.3: Piccolo F28035 ISO controlCARD

3.2.1 ADC Module

Based on the Texas Instruments' document [17], ADC is a single 12-bit converter with a 16-bit ADC register, which is fed by two sample and hold circuits. There are two different types of sampling modes:simultaneous and sequential sampling modes. The analog input range is from 0 V to 3.3 V, and it can have up to 16 inputs.

3.2.2 ePWM Module

The Pulse Width Modulation (PWM) strategy is used to chop the supply voltage. Because the PWM strategy has a fixed chopping frequency, the switching noises are much easier to filter. In this thesis, the chopping frequency of PWM is 20 kHz.

The ePWM module is a fundamental part in digital motor control. The ePWM module is able to generate PWM signals with minimal CPU usage [18].

For the BLDC motor control, three ePWM modules are needed to generate six PWM signals for the three-phase inverter.

In this thesis, one high side transistor is switched on and off according to the control signals, and one low side transistor is left on. This mode is able to reduce the switching losses and torque ripples.

3.3 DRV8312 Digital Motor Control Board

The DRV8312 DMC board is the motor driver board. The key component is the DRV8312 which is a three-phase motor driver. On the DRV8312 DMC board, some macros to implement different functions in the BLDC motor driver system are included. In this section, an introduction will be made to the DRV8312 DMC board based on the documents [15][16].

3.3.1 DRV8312

Because the BLDC motor is not self-commutated, the stator coils will be energized in a predefined order to make the rotor rotate. The stator coils needs to be powered by the external device. For a three-phase BLDC motor, normally a three-phase inverter is used to power the stator coils. Figure 3.1 shows the diagram of the inverter. The Piccolo F28035 controlCARD will send PWM control signals to the three-phase inverter.

DRV8312 is a three-phase BLDC motor driver in the Texas Instrument DRV83x2 driver family. The DRV8312 is able to be applied in the energy-efficient areas, because it has high energy efficiency which can reach maximum 97 %. In order to power DRV8312, two different power supplies are needed, one at 12 V for gate-drive voltage supply and power supply for digital voltage regulator, and another up to 50 V for power supply input for half-bridges [15].

The PWM switching operating frequency of the DRV8312 can be up to 500 kHz. This driver has an advanced protection system which can protect the device from different fault conditions that could make a damage to the hard-wares. The protection system includes the bootstrap capacitor undervoltage protection which can protect the device from the possible damage caused low

switching frequency operation, overload protection, and short circuit protection. The overcurrent detectors allow users to set the current limits based on the application requirements, and the current-limiting circuit will prevent the BLDC motor from possible damage caused by overcurrent.

3.3.2 Macro Blocks

On the DRV8312 DMC board, there are several macro blocks to implement different functions. The DC bus connection macro block provides DC bus power for the control board. There are two options for the connection block: one is using the power entry jack to connect a 24 V AC/DC supply, and another is using PVDD/GND terminals to connect a different power supply.

From Figure 3.1, the DRV8312 DMC board can be connected with a BLDC motor, and it can also receive the Hall-effect sensors or Quadrature Encoder signals. The motor connection block is to connect the BLDC motor wires [16]. The Quadrature Encoder connection block can be applied to connect a shaft encoder to receive motor positions information. Hall-effect sensor connection block can be used to connect to the Hall-effect sensors. In this thesis, the signals from the Hall-effect sensor connection block is applied to verify the accuracy of the sensorless commutation methods.

From Figure 3.1, the DRV8312 DMC board has the terminal voltage sensing block to measure the three phase terminal voltages V_a, V_b and V_c. The terminal voltages are measured by taking ground as the referenced point. The details about the terminal voltage sensing block will be introduced in Chapter 4. The current sensing block is to measure the BLDC motor currents. I_a, I_b and I_c are the phase currents, and I_{DC} are the DC bus current. In order to measure the motor current, a reference voltage of 1.65 V is required. This reference voltage can be provided by a voltage follower. On the DRV8312 DMC board, the voltage follower circuit is applied to generate a 1.65 V reference voltage from the 2.5 V voltage source.

A differential amplifier circuit is applied to convert the current input to an output voltage from 0 to 3.3 V. Figure 3.4 shows the differential amplifier circuit on the DRV8312 DMC board. The reference voltage 1.65 V is provided

by the voltage follower circuit. The transfer function of the circuit can be shown as:

$$V_{out} = 1.65 + I \cdot R_1 \cdot \frac{R_3}{R_2} = 1.65 + 0.191I \tag{3.1}$$

where V_{out} is the output voltage from the differential amplifier circuit, I is the motor current and R_1,R_2 and R_3 are the resistances in the differential amplifier circuit.

The transfer function is linear and the analog input range is from 0 V to 3.3 V. Because the current is bidirectional, which has both positive and negative currents, 0 V represents the minimum negative current and 3.3 V represents the maximum positive current. When the output voltage is 0 V, the current input is −8.65 A. When the output voltage is 3.3 V, the current input is 8.65 A. The output voltage range (0 V to 3.3 V) represents the measured phase current range (−8.65 A to 8.65 A).

When the current analog input is 3.3 V, the sampled ADC result value would be 4096. The range of ADC result is from 0 to 4096. Based on the ADC result, the current can be converted to the per unit format from −1.0 to 1.0. ±1.0 represents the measured motor current ±8.65 A.

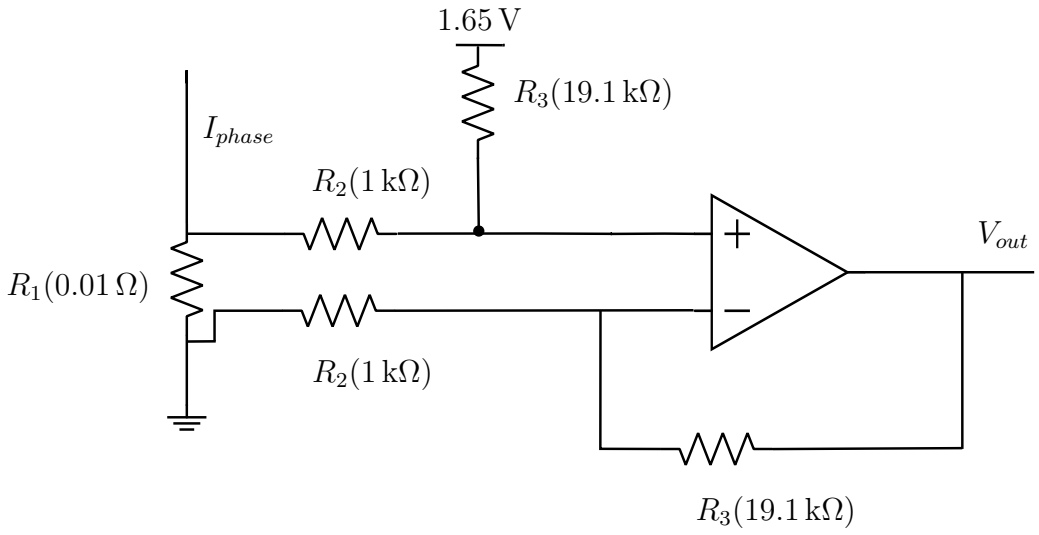

Figure 3.4: Differential amplifier circuit on DRV8312 DMC board

3.3.3 Power Domains of the Kit

There are two power domains on this kit. One is the low voltage domain, which is used to provide power for the F28035 C2000 controller and the logic circuits. The low voltage domain has three levels voltages: 3.3 V, 5 V and 12 V. The low voltage domain can be sourced from two areas: one is the 12 V DC control power entry, which needs external power supply, and another is the on board buck regular, which will regulate the DC bus power to 12 V.

Another power domain is the medium voltage power domain, which will provide medium voltages to the three-phase inverter. The medium voltages are called the DC bus voltages. The three-phase inverter will provide power to the BLDC motor and the medium voltages can be up to 52.5 V.

For each phase of the BLDC motor, an individual switch is used to determine the control mode of that phase. The switch can be manually set to three positions. If the switch is in the middle position, the switch will be controlled by a GPIO signal. If the switch is in the up position, the half-bridge output will be enabled. If the switch is in the down position, the half-bridge output will be disabled.

3.3.4 PWMDAC Module

The PWMDAC module can be applied to view the measurements waveforms on an oscilloscope. To get the actual low frequency signals, a first order low-pass filter is used to filter out the high frequency components. The PWMDAC module can be used to observe three different signals at one time. The low-pass filter time constant (τ) and cut-off frequency (f_c) can be calculated using following equations:

$$\tau = R \cdot C = 2.21 \times 10^{-4}\,\mathrm{s} \tag{3.2}$$

$$f_c = \frac{1}{2\pi\tau} = 720.5\,\mathrm{Hz} \tag{3.3}$$

where R is the low-pass filter resistance and C is the low-pass filter capacitance.

3.4 BLDC Motor

Figure 3.5 shows the BLDC motor used in this thesis, which is made by Anaheim Automation and its model number is BLY172S-24V-4000. This BLDC motor is a cost effective solution to the velocity control application. This motor has 4 pairs of rotor poles and three wires for the phases and five wires for the hall sensors. Table 3.1 shows the motor specifications.

Parameter	Values
P	8
R	$0.4\,\Omega$
L	$0.6\,\text{mHz}$
K_t	$0.041\,\text{Nm/A}$
K_e	$3.35\,\text{V/kRPM}$
J	$48\,\text{g}-\text{cm}^2$

Table 3.1: BLDC motor specifications

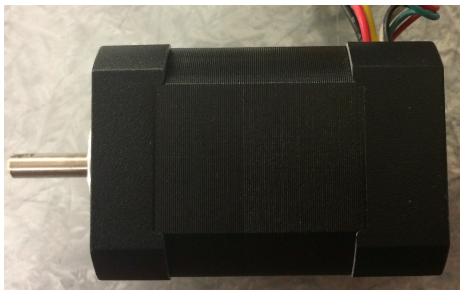

Figure 3.5: BLY172S-24V-4000 motor

3.5 Summary

In this chapter, we present the experimental environment in this thesis. An introduction is made to the Piccolo F28035 controlCARD, the DRV8312 DMC board and also the basic macro blocks. Finally, we make a discussion on the BLDC motor and its parameters.

Chapter 4

Sensorless BLDC Motor Drive Based on Line Voltage Differences

In this chapter, a sensorless BLDC motor control method based on line voltage differences [6] is introduced and verified through experiment. As introduced in Chapter 1, methods based on line voltage differences can eliminate the requirement for the motor neutral voltage, which will increase the accuracy of the commutation strategy.

4.1 Six-step Commutation

The six-step commutation is the most commonly used way to commutate a BLDC motor. Figure 4.1 shows the stator space sectors diagram. A and X represent the stator windings of phase A. B and Y represent the stator windings of phase B. C and Z represent the stator windings of phase C. $A-X$, $B-Y$ and $C-Z$ separate the space into six 60° sectors.

4.1.1 Analysis of Six-step Commutation

The six sectors represents six states of a BLDC motor. If Hall-effect sensors are used to detect rotor positions, for each of the six states, three-digit numbers based on the three Hall-effect sensors' signals are used to represent the current rotor position. When the rotor moves to the next sector, the three-digit numbers will change to a different set of three-digit numbers representing the

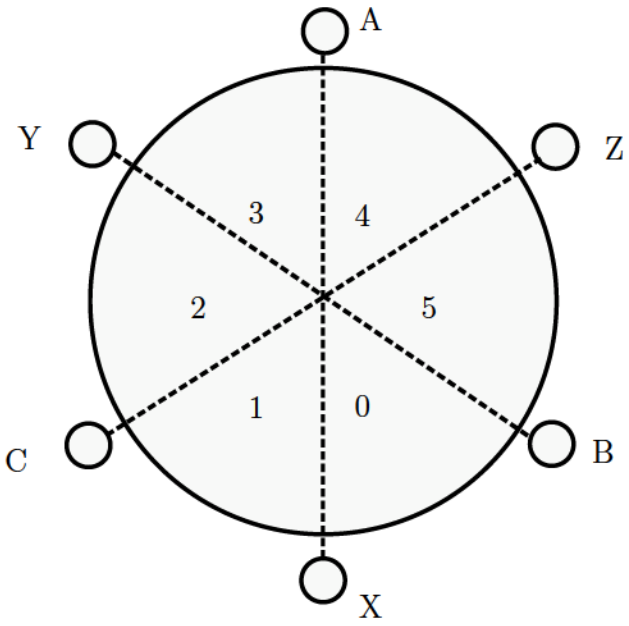

Figure 4.1: Stator space sectors diagram

new state. For sensorless control methods, different techniques will be used to estimate rotor positions.

Assuming that the rotor is in sector 0, the current direction of phase A is from A to X. the current direction of phase B is from Y to B and phase C is floating. Now the stator field is in the direction of $C - Z$ as shown in Figure 4.2(a), and it will will drive the rotor to move to sector 1.

After rotor moves into sector 1, the current direction of phase A is from A to X. the current direction of phase C is from Z to C and phase B is floating. The stator currents shape the stator field which is in the direction of $B - Y$ as shown in Figure 4.2(b). Torque will be generated based on the phase shift between the rotor field and the stator field. Then the torque will drive the rotor to move to sector 2.

In sector 2, the current direction of phase C is from Z to C. The current direction of phase B is from B to Y and phase A is floating. The stator field is in the direction of $A - X$ as shown in Figure 4.2(c), and it will drive the rotor to move to sector 3.

In sector 3, the current direction of phase A is from X to A. The current direction of phase B is from B to Y and phase C is floating. The stator field

is in the direction of $C - Z$ as shown in Figure 4.2(d), and it will will drive the rotor to move to sector 4.

In sector 4, the current direction of phase A is from X to A. The current direction of phase C is from C to Z and phase B is floating. The stator field is in the direction of $B - Y$ as shown in Figure 4.2(e), and it will drive the rotor to move to sector 4.

In sector 5, the current direction of phase C is from C to Z. The current direction of phase B is from Y to B and phase A is floating. The stator field is in the direction of $A - X$ as shown in Figure 4.2(f), and it will drive the rotor to move to sector 0.

As analyzed above, the stator field moves in a discrete step of 60 electrical degrees. The torque will continuously drive the rotor to rotate. Because the phase shift between the rotor field and the stator field will change when the rotor is rotating, this shift will cause torque ripples. The torque ripples can be reduced if the field oriented control is applied. Then the phase shift between the rotor field and the stator field is fixed to be 90 electrical degrees to generate the maximum torque.

The commutation state pointer input (0 to 5) indicates one of the six states. During each state, only two phases are conducting so two switches are active and the other four will be turned off. If the commutation state pointer is equal to 0, current flows from phase A to phase B. Table 4.1 shows the six commutation states of the BLDC motor.

Commutation States	i_a	i_b	i_c
0	positive	negative	floating
1	positive	floating	negative
2	floating	positive	negative
3	negative	positive	floating
4	negative	floating	positive
5	floating	negative	positive

Table 4.1: Commutation states in six-step BLDC motor control

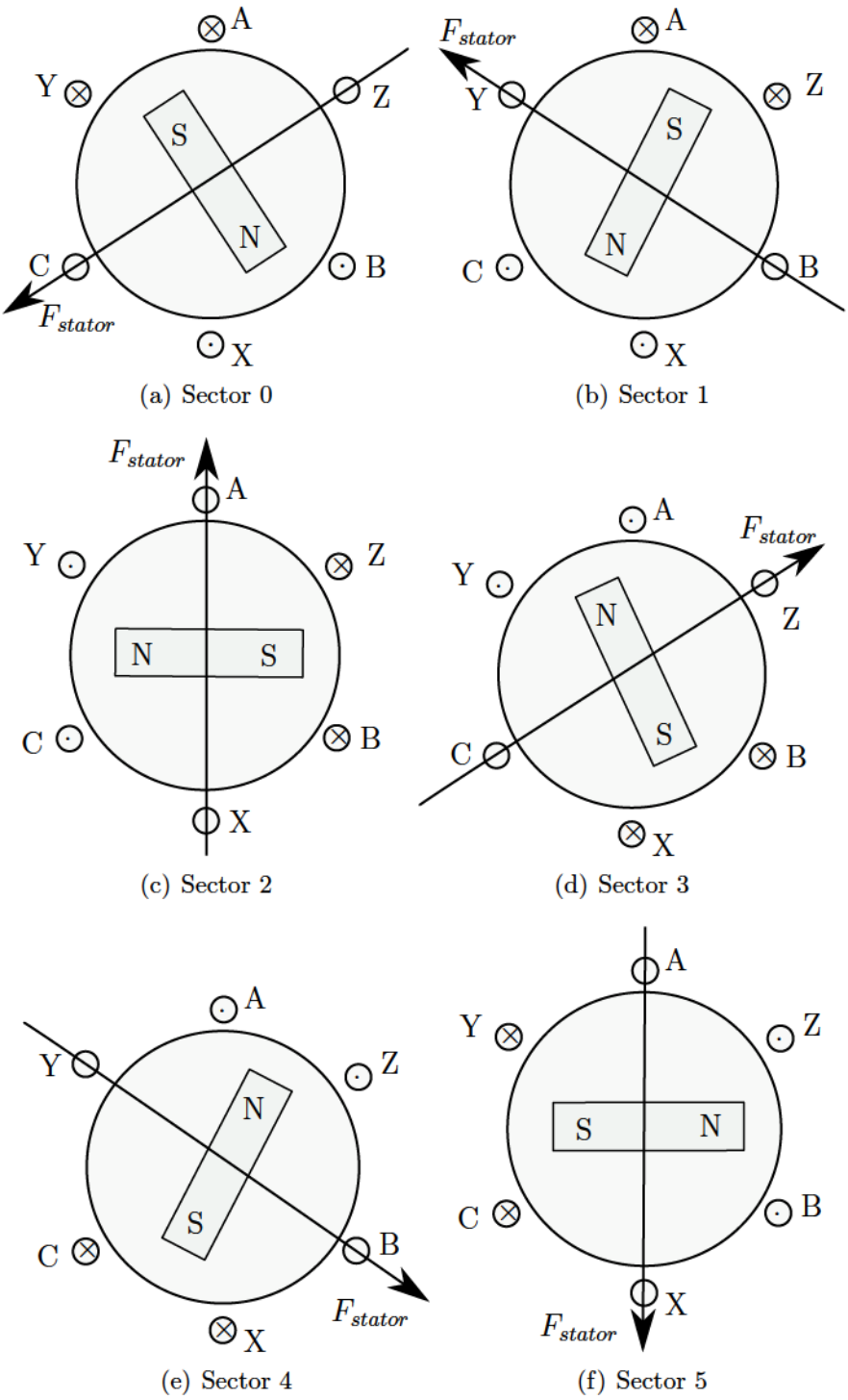

Figure 4.2: BLDC motor six-step commutation

4.2 Sensorless Commutation Method Based on Line Voltage Differences

In this section, a sensorless control method using the six-step commutation sequence will be introduced. The proposed method are based on the work in [6].

For the BLDC motor we used, stator windings of three phases are connected in star. The terminal voltage of phase A referenced with the motor neutral voltage is V_{an} as:

$$V_{an} = Ri_a + L\frac{\mathrm{d}i_a}{\mathrm{d}t} + e_a \tag{4.1}$$

Similarly, terminal voltages of phase B and phase C are V_{bn} and V_{cn} as:

$$V_{bn} = Ri_b + L\frac{\mathrm{d}i_b}{\mathrm{d}t} + e_b \tag{4.2}$$

$$V_{cn} = Ri_c + L\frac{\mathrm{d}i_c}{\mathrm{d}t} + e_c \tag{4.3}$$

where V_{an}, V_{bn} and V_{cn} are the phase voltages referenced to the motor neutral voltage, L is the phase stator inductance, R is the phase stator resistance, i_a, i_b and i_c are the phase currents and e_a, e_b and e_c are the phase back-EMFs.

On DRV8312 DMC board, the terminal voltages are measured by taking ground as the referenced point. The line voltage V_{ab} of the terminal voltages can be calculated as:

$$V_{ab} = R(i_a - i_b) + L\frac{\mathrm{d}(i_a - i_b)}{\mathrm{d}t} + e_a - e_b \tag{4.4}$$

Similarly, terminal line voltages V_{bc} and V_{ca} are shown below:

$$V_{bc} = R(i_b - i_c) + L\frac{\mathrm{d}(i_b - i_c)}{\mathrm{d}t} + e_b - e_c \tag{4.5}$$

$$V_{ca} = R(i_c - i_a) + L\frac{\mathrm{d}(i_c - i_a)}{\mathrm{d}t} + e_c - e_a \tag{4.6}$$

From equations above, the line voltages can be calculated based on the terminal voltages measured with respect to ground, so the requirement for motor neutral voltage is eliminated.

We can calculate the line voltage differences based on the line voltages equations above. The line voltage difference V_{bcab} can be calculated as:

$$\begin{aligned} V_{bcab} &= V_{bc} - V_{ab} \\ &= R(2i_b - i_a - i_c) + L\frac{\mathrm{d}(2i_b - i_a - i_c)}{\mathrm{d}t} + 2e_b - e_a - e_c \end{aligned} \tag{4.7}$$

Similarly, V_{abca} and V_{cabc} can be calculated as:

$$\begin{aligned} V_{abca} &= V_{ab} - V_{ca} \\ &= R(2i_a - i_b - i_c) + L\frac{\mathrm{d}(2i_a - i_b - i_c)}{\mathrm{d}t} + 2e_a - e_b - e_c \end{aligned} \tag{4.8}$$

$$\begin{aligned} V_{cabc} &= V_{ca} - V_{bc} \\ &= R(2i_c - i_a - i_b) + L\frac{\mathrm{d}(2i_c - i_a - i_b)}{\mathrm{d}t} + 2e_c - e_a - e_b \end{aligned} \tag{4.9}$$

If the commutation state pointer is equal to 0, the stator current flows from phase A to phase B. Because phase C is open, the phase C current $i_c = 0$. Phase A current i_a and phase B current i_b have the same magnitude but opposite. From Figure 2.1 [23], phase A back-EMF e_a and phase B back-EMF e_b also have the same magnitude but opposite. The relationships can be shown as:

$$i_a + i_b = 0 \tag{4.10}$$

$$e_a + e_b = 0 \tag{4.11}$$

When the commutation state pointer is equal to 0, the line voltage difference V_{cabc} can be calculated as:

$$V_{cabc} = V_{ca} - V_{bc} = 2e_c - e_a - e_b = 2e_c \tag{4.12}$$

From the equation above, the line voltage difference V_{cabc} is equal to an amplified phase C back-EMF value and the gain is two. So we can use line voltage differences to estimate zero-crossing points of back-EMFs. Theoretically, when the commutation state pointer is equal to 0, V_{cabc} starts from the maximum positive value and goes to the minimum negative value. Because the back-EMF waveform changes linearly, the zero-crossing point will occur in the middle of the commutation state 0. As each state contains 60 electrical degrees, a 30° offset exists between the back-EMFs' zero-crossing points and the current commutation instants.

Similarly, when the commutation state pointer is equal to 3, the stator current flows from phase B to phase A and phase C is open. V_{cabc} has the same expression as in commutation state 0. The difference is that V_{cabc} starts from the minimum negative value and goes to the maximum positive value.

In commutation state 1, the stator current flows from phase A to phase C, and phase B is open. In commutation state 4, the stator current flows from phase C to phase A and phase B is open. The phase B current $i_b = 0$. Phase A current i_a and phase C current i_c are equal and opposite. Phase A back-EMF e_a and phase C back-EMF e_c are also equal and opposite. The line voltage difference V_{bcab} can be calculated as:

$$V_{bcab} = V_{bc} - V_{ab} = 2e_b - e_a - e_c = 2e_b \tag{4.13}$$

In commutation state 2, the stator current flows from phase B to phase C, and phase A is open. In commutation state 5, the stator current flows from phase C to phase B, and phase A is open. The phase A current $i_b = 0$. Phase B current i_b and phase C current i_c are equal and opposite. Phase B back-EMF e_b and phase B back-EMF e_c are also equal and opposite. The line voltage difference V_{abca} can be calculated as:

$$V_{abca} = V_{ab} - V_{ca} = 2e_a - e_b - e_c = 2e_a \tag{4.14}$$

To validate the proposed sensorless method, the relationship between the line voltage differences and back-EMFs is verified in Matlab/Simulink environment. For a real BLDC motor, the back-EMF waveform shape cannot be ideal trapezoidal, which is the reason why the back-EMF voltage constant is less than the torque constant for the BLDC motor used in the experimental environment. The BLDC motor model for simulation has ideal trapezoidal back-EMFs, and we choose the the torque constant to be same as the back-EMF voltage constant instead of the one in Table 3.1. Except for the torque constant, the BLDC motor in the Simulink model has the same parameters in Table 3.1.

The line voltage differences are represented by the expressions of back-EMFs to validate the zero-crossing points match. Figure 4.3 shows the simulation results of the line voltage differences and back-EMFs waveforms. From

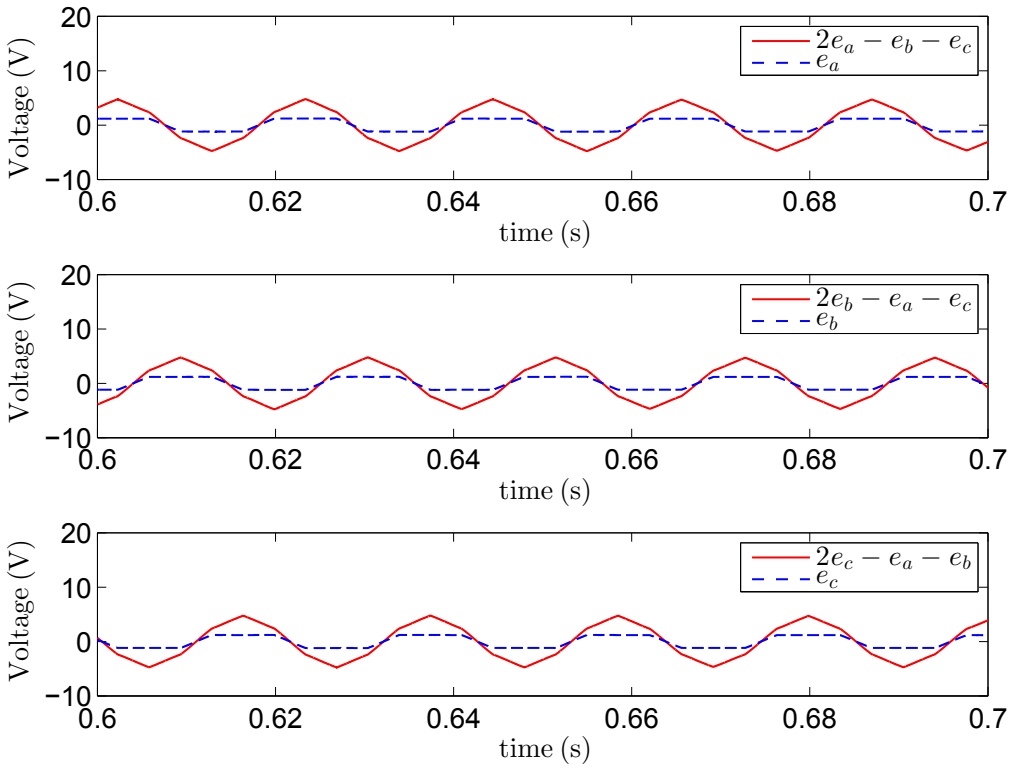

Figure 4.3: Simulations results of the line voltage differences and back-EMFs waveforms at 700 rpm with 0.04 Nm load

the simulation results, we can see that at the zero-crossing points, the corresponding line voltage difference is an amplified back-EMF, and the line voltage differences have the same zero-crossing points as the back-EMFs.

In each state, one line voltage difference is applied to estimate the zero-crossing points of the corresponding back-EMF waveform. A combined commutation function is applied to estimate all the zero-crossing points of back-EMFs as shown in Table 4.2. Table 4.2 also shows the polarity of the zero-crossing points.

The combined commutation function can be shown in Figure 4.4. The simulation results show that the combined commutation function has the same zero-crossing points as the back-EMFs, which verifies the correctness of the combined commutation function. The combined commutation function will be applied in the experiment environment.

Commutation States	Commutation Function	Polarity of Zero-crossing Points
0	V_{cabc}	$+V_{max}$ to $-V_{min}$
1	V_{bcab}	$-V_{min}$ to $+V_{max}$
2	V_{abca}	$+V_{max}$ to $-V_{min}$
3	V_{cabc}	$-V_{min}$ to $+V_{max}$
4	V_{bcab}	$+V_{max}$ to $-V_{min}$
5	V_{abca}	$-V_{min}$ to $+V_{max}$

Table 4.2: Commutation sequence for the method based on line voltage differences

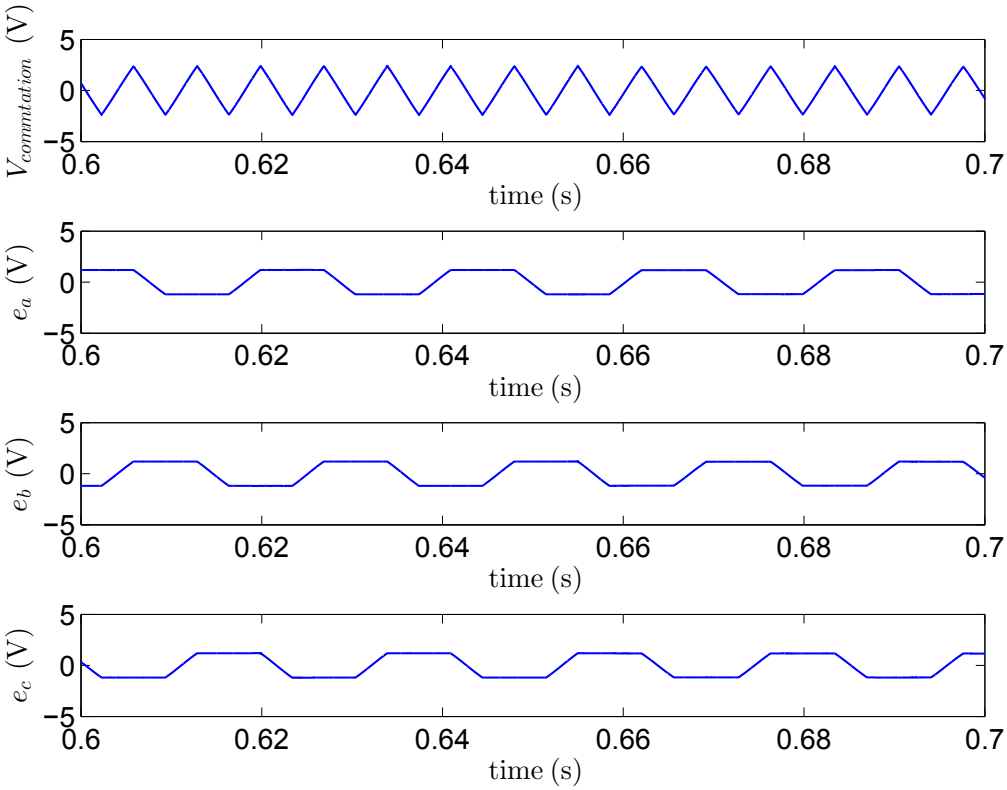

Figure 4.4: Simulations results of the combined commutation function and back-EMFs waveforms at 700 rpm with 0.04 Nm load

4.3 Voltage Measurement

ADC modules convert the analog signals to digital signals. The analog input range of the ADC module is from 0 V to 3.3 V but BLDC motor terminal voltages are much higher than 3.3 V, so a voltage resistor divider circuit is

used to convert the terminal voltage to fit the analog input range of ADC module.

Because of the inverter switching, BLDC motor terminal voltages contain some high frequency harmonics. In order to eliminate the harmonics, a first-order low pass filter is included in the voltage resistor divider circuit as shown in Figure 4.5.

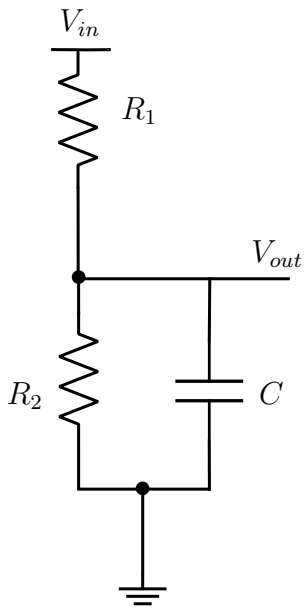

Figure 4.5: Voltage resistor divider circuit

The transfer function of the low pass filter is:

$$\frac{V_{out}}{V_{in}} = \frac{R_2}{R_1 + R_2 + R_1 R_2 C s} \tag{4.15}$$

where C is the low pass filter capacitance, R_1 and R_2 are the voltage divider resistances, V_{out} is the filtered waveform of V_{in}.

Table 4.3 shows the parameters of the motor terminal voltage sensing circuit.

4.4 Phase Delay Compensation

From the analysis above, line voltage differences can be used to estimate the zero-crossing points of back-EMFs. Because a 30° offset exists between the

Parameter	Values
R_1	95.3 kΩ
R_2	4.99 kΩ
C	0.047 µF

Table 4.3: Terminal voltage sensing circuit specifications

back-EMFs' zero-crossing points and the current commutation instants, a 30° phase shift should be made to ensure the correct operation of the motor.

However, because of the phase delay caused by the low pass filter, the actual offset between the measured zero-crossing point of back-EMFs and current commutation instants is not exactly 30°. The delayed angle caused by the first-order low pass filter can be calculated as:

$$\theta = -\tan^{-1}\left(\frac{R_1 \cdot R_2 \cdot C \cdot \omega_e}{R_1 + R_2}\right) \tag{4.16}$$

$$\omega_e = \frac{2\pi}{T} \tag{4.17}$$

where T is one electrical period and ω_e is the synchronous speed of the BLDC motor.

Due to the delayed angle caused by the low pass filter, the electrical degree offset ϕ between the zero-crossing points of back-EMFs and current commutation instants should be modified as

$$\phi = 30° - \theta \tag{4.18}$$

Figure 4.6 shows the software flowchart of the proposed sensorless commutation method with phase delay compensation. In order to calculate the ϕ in software, the electrical period needs to be calculated. As the current electrical period is unknown, the difference between two adjacent electrical periods is small enough to ignore, so the last electrical period T is applied to calculate T_{delay}. At the beginning of state 5, T will be calculated based on the time difference between the current time and the beginning time of state 5 in the last electrical period. The phase delay time will be calculated and then used in the next electrical period:

$$T_{delay} = \frac{\phi}{360} \cdot T \tag{4.19}$$

where T is the last electrical period and ϕ is the phase delay angle calculated at the end of last electrical period.

For each commutation state, the time counter will start after detecting the zero-crossing point of the corresponding line voltage difference. When the time counter is equal to T_{delay}, this point is treated as the commutation instant and the BLDC motor will switch to the next state.

As mentioned in Chapter 2, the relationship between electrical frequency and mechanical frequency is

$$f_e = \frac{p}{2} f_m \tag{4.20}$$

$$f_m = \frac{N_{rpm}}{60} \tag{4.21}$$

where p is the number of poles, f_m is the mechanical frequency, f_e is the electrical frequency and N_{rpm} is rotor speed in rpm.

The electrical period T from the commutation method will be applied to estimate N_{rpm} as shown in equation below:

$$\begin{aligned} N_{rpm} &= 60 f_m = 60 \cdot \frac{2}{p} f_e \\ &= \frac{120}{Tp} \end{aligned} \tag{4.22}$$

From the analysis above, the delayed angle caused by the low pass filter has a positive relationship with the motor rotor speed. If the BLDC motor speed is 1000 rpm, the delayed angle caused by the low pass filter is 5.33° using the equation below:

$$\begin{aligned} \theta &= \tan^{-1}\left(\frac{R_1 \cdot R_2 \cdot C \cdot \omega_e}{R_1 + R_2}\right) \\ &= \tan^{-1}\left(\frac{R_1 \cdot R_2 \cdot C}{R_1 + R_2} \cdot \pi p \frac{N_{rpm}}{60}\right) \end{aligned} \tag{4.23}$$

When the speed is low or medium, the delayed angle won't cause a commutation mistake. But when motor speed is high, the delayed angle will cause problems. Some compensation needs to be done to guarantee the correct operation of BLDC motors. In this thesis, F28035 C2000 controller will be used to compensate the phase delay ϕ, so the current commutation instants can be in phase with the zero-crossing points of line voltage differences.

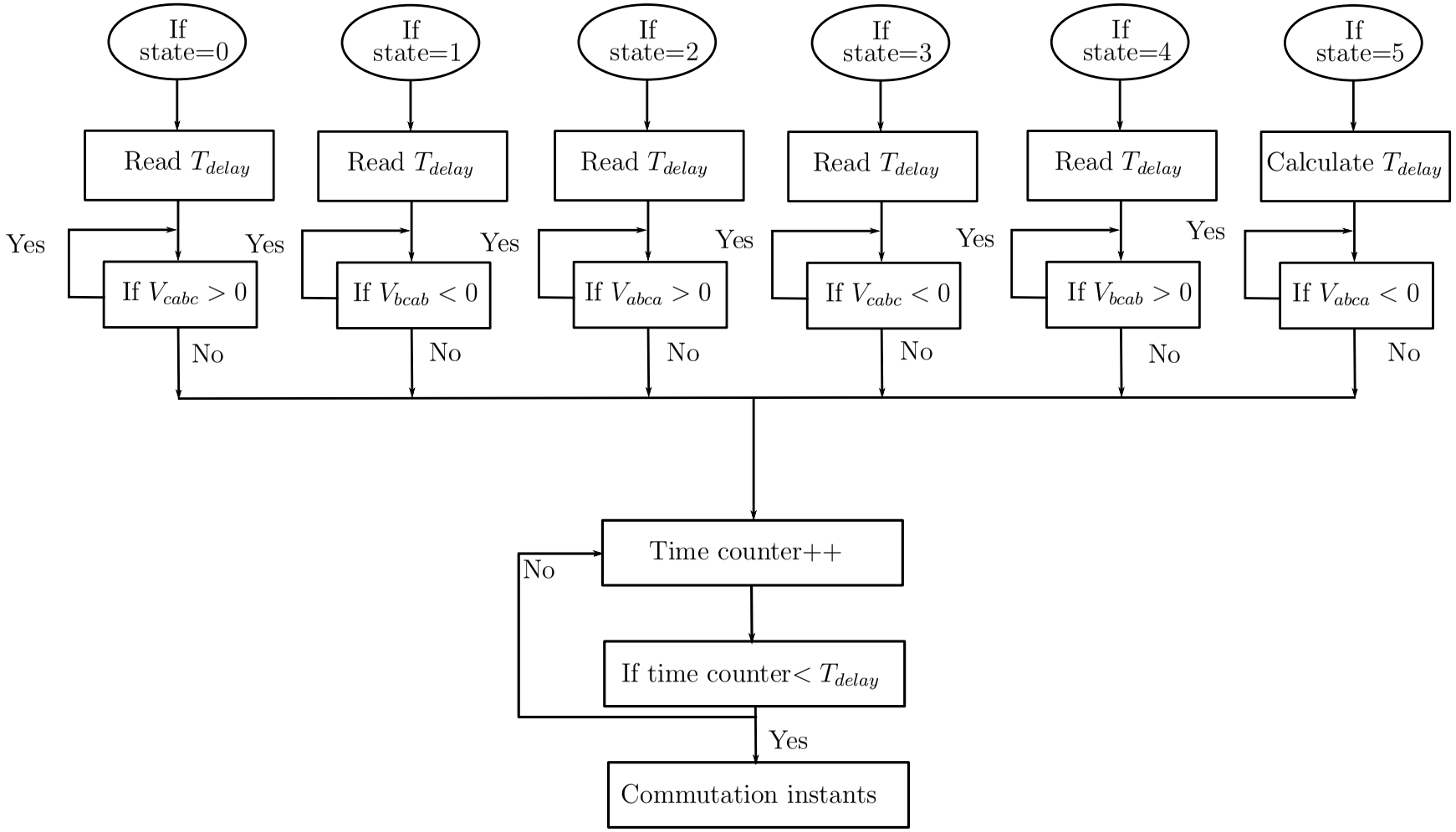

Figure 4.6: Software flowchart of the sensorless commutation method based on line voltage differences

4.5 Starting Procedure

For BLDC control methods with Hall-effect sensors or Quadrature Encoder signals, it is not a problem for a BLDC motor to start up. For back-EMF based methods like the method used in this chapter, back-EMFs' values are needed to achieve the position estimation. However, back-EMFs' values are zero during standstill, and they are also very small when the motor speed is low.

Normally, a starting procedure is required for the methods based on back-EMFs. In this chapter, the BLDC motor will be started blindly using the conventional open-loop starting method [8].

During the first stage, any two phases of stator windings will be energized. In this thesis, the stator current will firstly flow from phase A to phase B. The stator currents will generate a flux whose amplitude and direction are both constant. The stator flux will attract the rotor to point in the same direction, so the rotor is forced to align at a predefined position [8]. Then, the stator current flows from phase A to phase C so the BLDC motor will be in the next state. The stator flux will point to a new direction, so the rotor will be attracted to move to the next position. During this open-loop starting mode, the stator windings will be energized in a predefined order:

$$AB \rightarrow AC \rightarrow BC \rightarrow BA \rightarrow CA \rightarrow CB$$

When the BLDC motor speeds up, back-EMFs will also increase. When the zero-crossing points of back-EMFs can be stably detected, the control system will switch to the sensorless mode.

4.6 Electrical Noises

The noises included in the calculated line voltage difference waveforms may cause false zero-crossing points detection. The main noises are from the chopped pulses generated by PWM. Spikes caused by the free-wheeling diode conduction current are another source [6].

Assuming that the BLDC motor is in commutation state 1, now it will switch to state 2. During commutation state 1, the upper transistor of phase A (T_1) and the lower transistor of phase C (T_6) are on. At the commutation instant, T_1 will be turned off and the upper transistor of phase B (T_3) will be turned on. The stator current continues to flow through the free-wheeling diode of phase A and decreases.

The free-wheeling current will cause spikes in the calculated line voltage difference waveforms. The spikes may cross the zero thus cause false zero-crossing points detection.

According to the reference [6], the free-wheeling current during time is much smaller than the phase delay time T_{delay}, so the spike will disappear before the back-EMFs cross zero.

The calculated line voltage difference waveforms also contains noises from the sensing circuit. For DRV8312-C2 kit, each terminal voltage is sensed with a voltage resistor divider and a first order low pass filter. The sensing circuit may bring noises to the measured terminal voltages so it will also affect the line voltage differences.

Because the virtual neutral voltage is not used in this method, it will reduce the affect of electrical noises. The low pass filter of the terminal voltage sensing circuit can filter out the chopped pulses generated by PWM, but the calculated line voltage difference waveforms still contain some noises which may cause false zero-crossing points detection. In order to minimize the influence of the noises, a counter can be used to calculate how many times the measured line voltage difference value crosses zero [38]. The noises only remain for a very short time. If the counter reaches a predefined value, this point is treated as the real zero-crossing point of the line voltage difference. Otherwise, it will be treated as noises and will not trigger the commutation to the next state.

4.7 Proposed Sensorless Drive

Assuming that $\hat{\omega}$ is the estimated motor speed and ω_{ref} is the reference motor speed, a proportional integral (PI) controller is applied to determine the duty

cycle of the PWM signals based on the difference between $\hat{\omega}$ and ω_{ref}. Figure 4.7 shows the proposed sensorless drive for speed control of a BLDC motor.

The measured three phase terminal voltages are the inputs of the line voltage differences calculation block. The calculated line voltage differences and the motor speed are the inputs of the commutation trigger block. At the beginning of each electrical period, the phase delay time will be calculated, and it will be used in this electrical period.

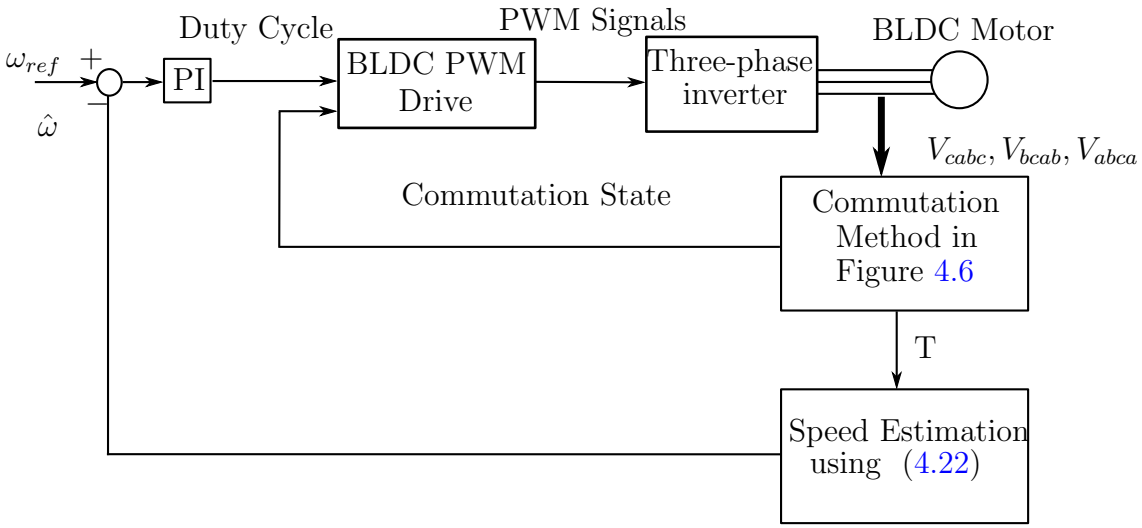

Figure 4.7: Proposed sensorless BLDC motor drive based on line voltage differences

4.8 Experimental Results

In this section, we presents the experiment results of the proposed sensorless BLDC motor drive based on line voltage differences at different speeds, and the effectiveness of the compensation method is also verified and analyzed.

4.8.1 Experiment Results at 600 rpm

Figure 4.8 shows the measured line voltage differences at 600 rpm. Figure 4.9 shows the speed response at 600 rpm, and the error is calculated using the equation below:

$$error(\%) = \frac{|\hat{\omega} - \omega_{ref}|}{\omega_{ref}} \times 100\% \tag{4.24}$$

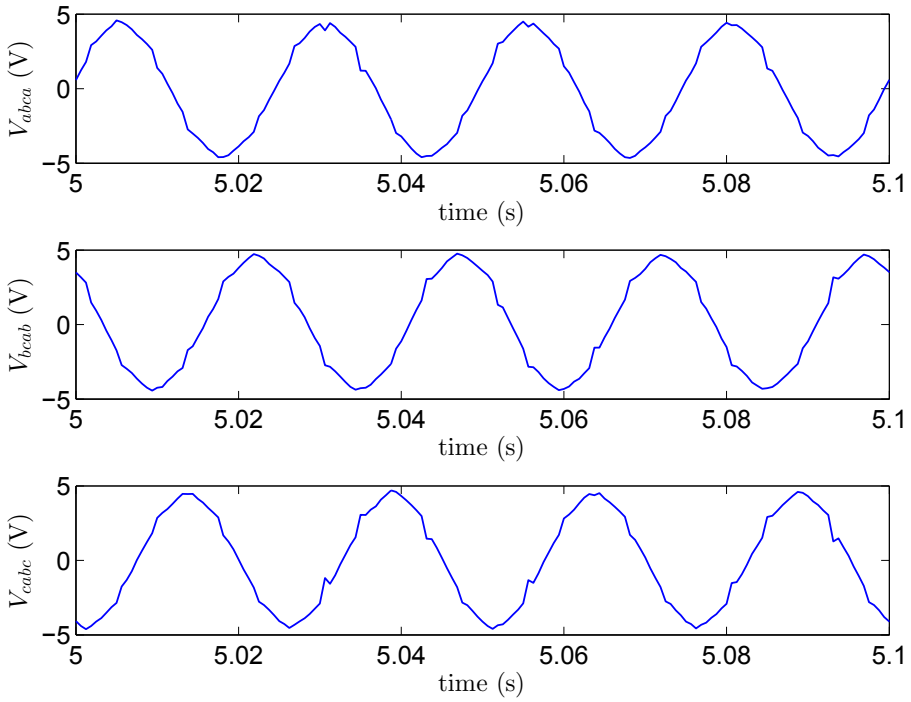

Figure 4.8: Experiment results of line voltage differences at 600 rpm

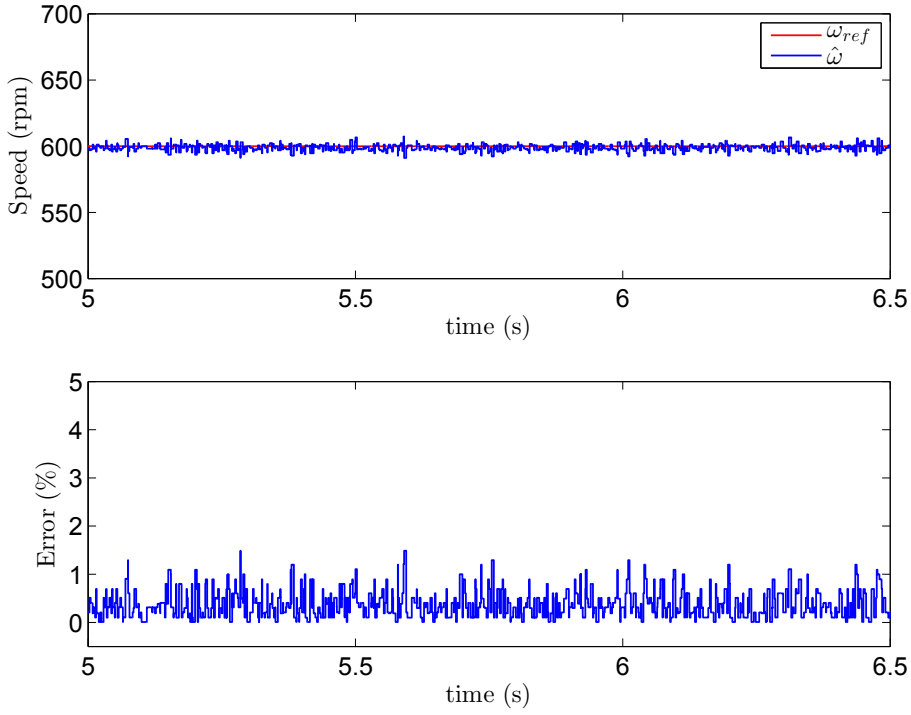

Figure 4.9: Speed response at 600 rpm

4.8.2 Experiment Results at 1000 rpm

Figure 4.10 shows the measured line voltage differences at 1000 rpm. Figure 4.11 shows the speed response at 1000 rpm.

Based on the results in subsection 4.8.1 and subsection 4.8.2, we can see that the line voltage differences waveforms are symmetric, and the speed of the BLDC motor can remain stable with negligible error.

When the BLDC motor runs in open-loop commutation mode, there is a big acoustic noise from the motor due to its inaccuracy commutation. During the sensorless commutation mode, the acoustic noise is reduced.

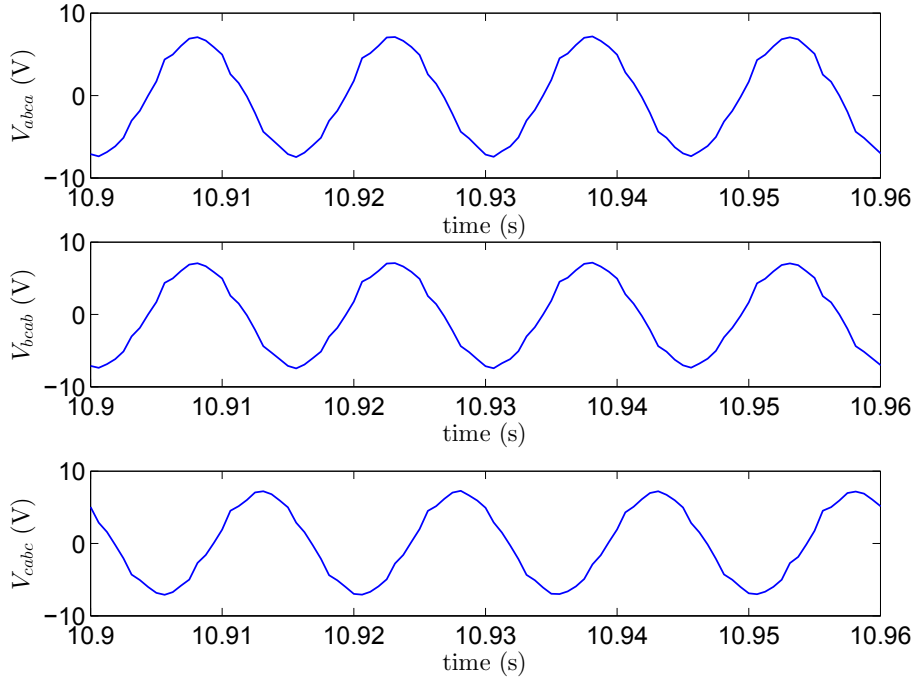

Figure 4.10: Experiment results of line voltage differences at 1000 rpm

4.8.3 Phase Delay Compensation

For the trapezoidal control of BLDC motors, back-EMFs are required to be in phase with the phase current. In this section, we will make comparison of the proposed sensorless drive with and without phase delay compensation. From the experiment results, the phase delay compensation method does not make a big difference if the BLDC motor works in low or medium speeds. However,

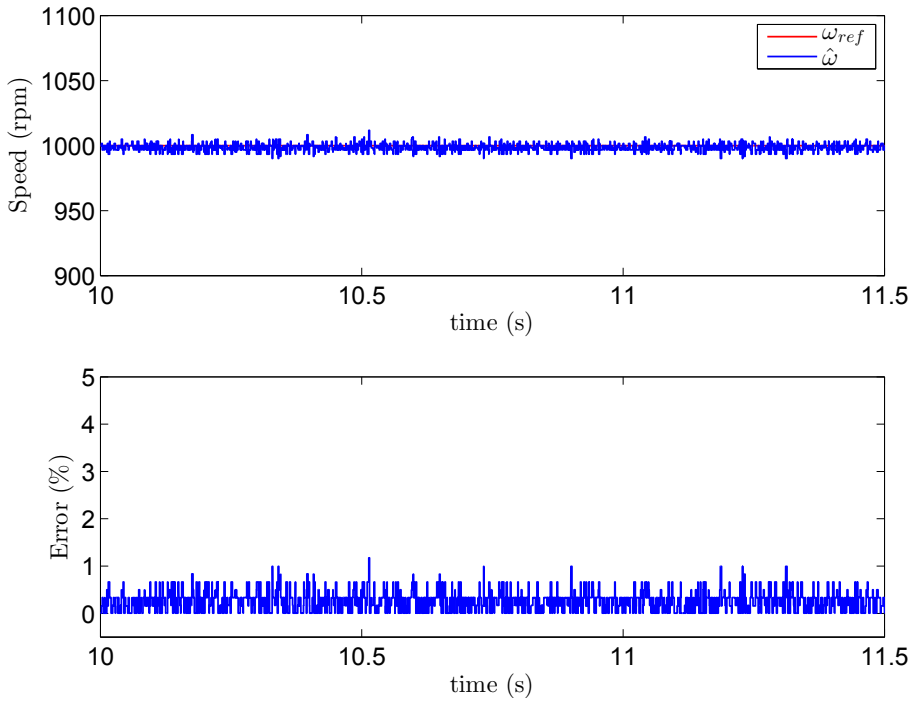

Figure 4.11: Speed response at 1000 rpm

when the BLDC motor speed is high, the effectiveness of the compensation method will be obvious.

In this section, we presents the experiment results at 1800 rpm. Because three phases are symmetric, the experiment results of phase A is analyzed to show the correctness of the compensation method. Figure 4.12 shows the relationship between phase A current i_a and V_{abca}. We can see that the commutation points of i_a lags 30° behind the zero-crossing points of V_{abca}. Figure 4.13 shows the speed response at 1800 rpm.

For the sensorless drive without phase delay compensation, the motor stalls when its speed is over 1800 rpm, because of the significant phase delay error (over 9.53°) caused by the low pass filter. To verify the effectiveness of the compensation method, Figure 4.14 shows the experiment results of the relationship between the ideal commutation signal (Hall-effect sensor A output) and the estimated commutation signal (virtual Hall-effect sensor A output obtained from the sensorless commutation method) at 1800 rpm.

From Figure 4.14, we can see that the estimated commutation signal lags

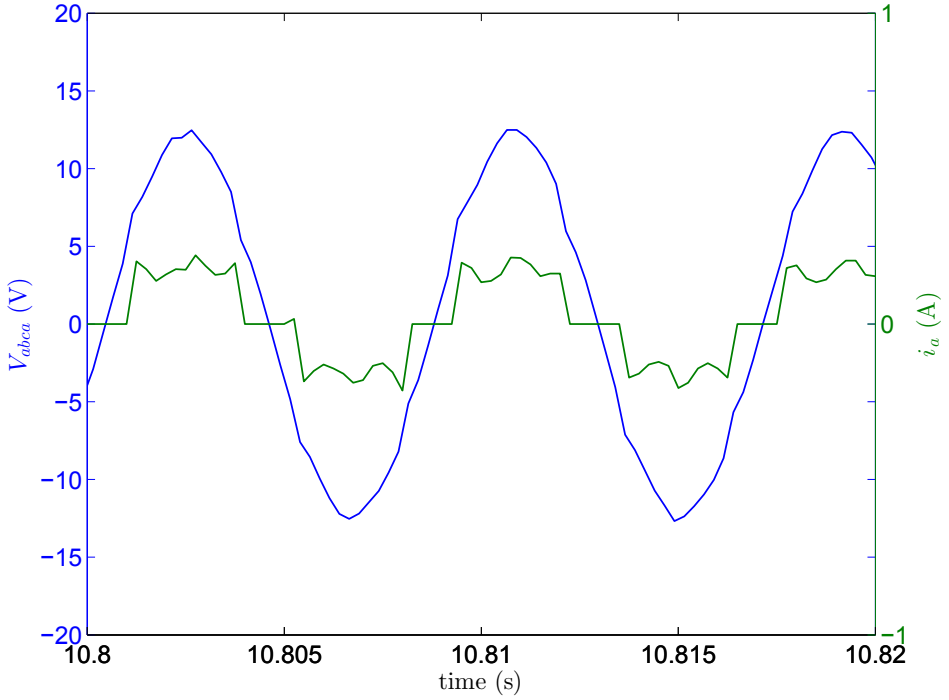

Figure 4.12: Phase A current and V_{abca} at 1800 rpm

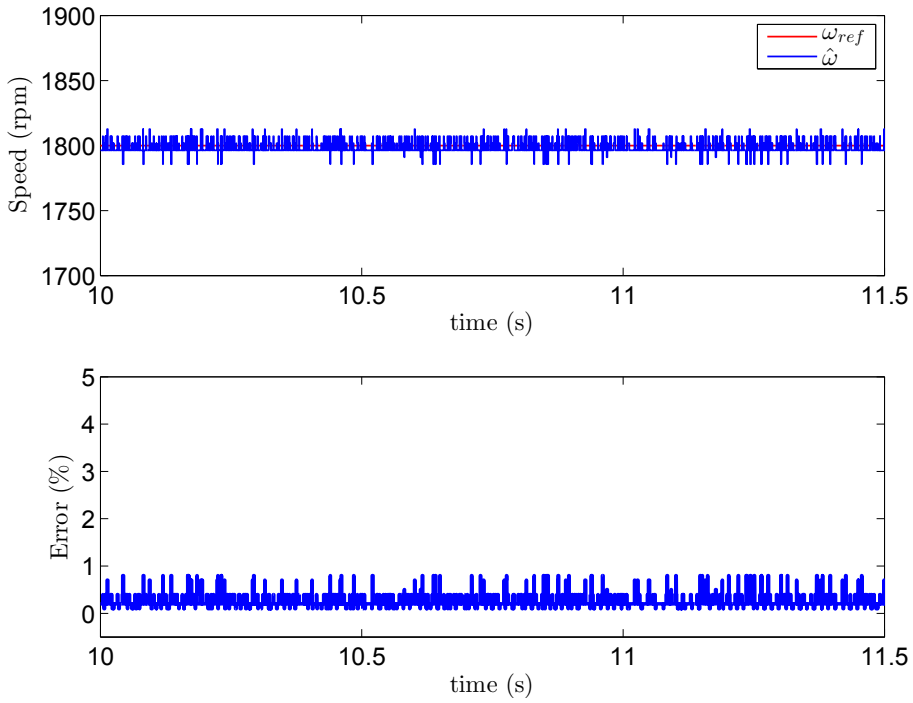

Figure 4.13: Speed response at 1800 rpm

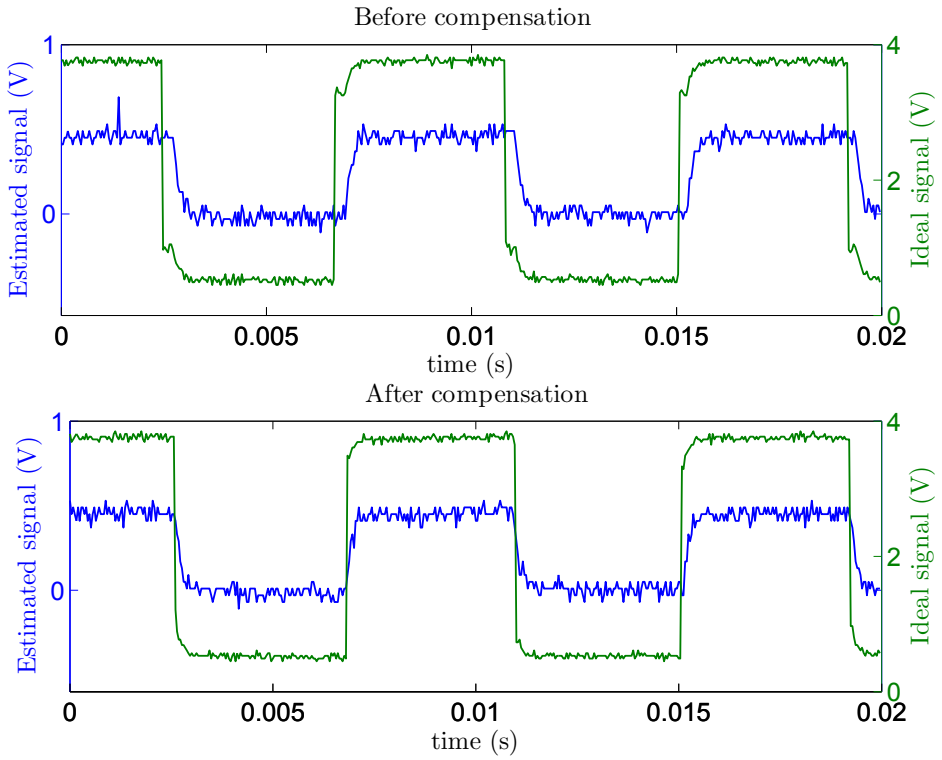

Figure 4.14: Ideal commutation signal and estimated commutation signal at 1800 rpm

behind the ideal commutation signal and the phase delay is significant. After phase delay compensation, the estimated commutation signal matches well with the ideal commutation signal.

Before phase compensation, the acoustic noise is noticeable due to inaccuracy commutation. After phase compensation, the acoustic noise is reduced.

Based on the analysis above, we can conclude that phase delay compensation is necessary for high speed region. With phase delay compensation, the high speed capability of BLDC motors can be improved, and the acoustic noise from the motor will be reduced. The estimated commutation signal is precise enough to replace the ideal commutation signal, so it can be applied to realize sensorless commutation.

4.9 Summary

In this chapter, we make a detailed analysis on the six-step commutation of the BLDC motors. Then we discuss the sensorless commutation method based on line voltage differences, and it is validated by the simulation results. The sensorless commutation method with phase delay compensation is further implemented in the experimental environment.

Chapter 5

Sensorless BLDC Motor Drive Based on Disturbance Observer

In Chapter 4, a sensorless control method based on terminal line voltage differences is introduced and verified through experiment. However, this sensorless method requires a 30° phase shift to acquire the correct commutation instants, which lowers the accuracy of the commutation method. The complexity of the sensorless control method is also increased. In this chapter, a sensorless control method based on the disturbance observer will be discussed, and this method does not require a 30° phase shift [39].

5.1 Disturbance Observer

The disturbance observer has been widely applied in the motion control area because of its ability to implement disturbance rejection and compensate the plant uncertainties. The Disturbance Estimating Filter (DEF) disturbance observer is introduced in [33].

The DEF disturbance observer is proposed based on the two-degree-of-freedom controller. For the two-degree-of-freedom controller, one degree-of-freedom is to implement disturbance rejection, and another is to design the reference response. The normal structure of DEF disturbance observer is shown in Figure 5.1 [33]. The actual plant transfer function is $P'(s)$ and the nominal plant transfer function is $P(s)$.

u_i is the input signal and d is the disturbance signal. The actual input

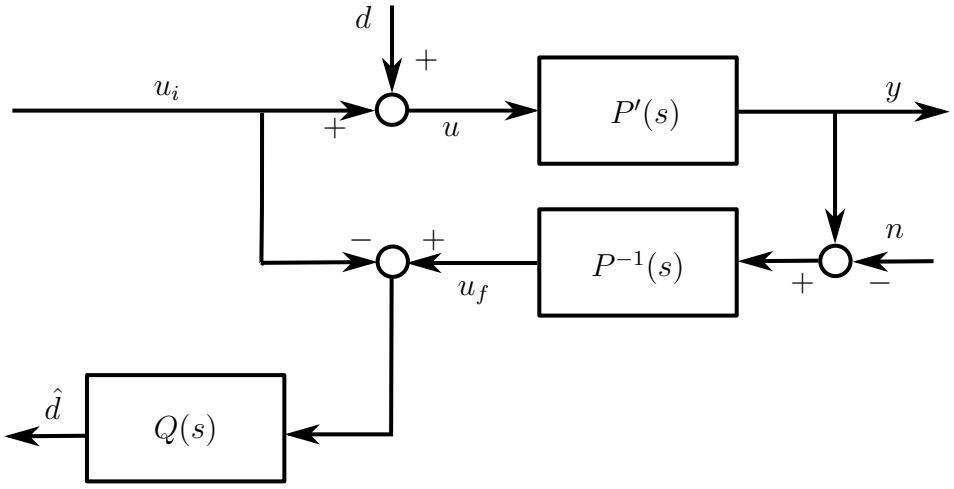

Figure 5.1: Structure of DEF disturbance observer

signal u is the superposition result of u_i and d. The output of the actual plant model is y, and n is the measurement noise. The function of y is shown as:

$$y = u \cdot P'(s) = (u_i + d) \cdot P'(s) \tag{5.1}$$

The inverse of nominal plant transfer function is $P^{-1}(s)$. The superposition result of y and n will be passed to $P^{-1}(s)$ to get the estimated input of the actual plant model u_f. The calculation function of u_f is shown below:

$$\begin{aligned} u_f &= (y - n) \cdot P^{-1}(s) \\ &= (u_i + d) \cdot P'(s) \cdot P^{-1}(s) - n \cdot P^{-1}(s) \end{aligned} \tag{5.2}$$

If there is no modeling error, $P'(s)$ and $P(s)$ are equal as:

$$P'(s) = P(s) \tag{5.3}$$

u_f can be simplified as:

$$u_f = u_i + d - n \cdot P^{-1}(s) \tag{5.4}$$

The difference between u_i and u_f is called the lumped disturbance [5]. From the equation above, we can see that the lumped disturbance contains the measurement noise n, which may affect the performance of the disturbance

observer. The frequency of the measurement noise is usually high, and the frequency of disturbance signal is low [5].

A low pass filter $Q(s)$ is required in the disturbance observer to filter out the measurement noise. For the $Q(s)$, its magnitude should be designed with the following characteristics [33]:

$$|Q(s)| \approx 1, \text{ in the low frequency range} \tag{5.5}$$

$$|Q(s)| \approx 0, \text{ in the high frequency range} \tag{5.6}$$

The filtered lumped disturbance $\hat{d}$ is the estimated disturbance signal by the disturbance observer.

$$\hat{d} = d \cdot Q(s) \tag{5.7}$$

The estimated disturbance signal by the disturbance observer $\hat{d}$ can be fed back to implement disturbance rejection.

5.2 Sensorless Commutation Method Based on Disturbance Observer

Figure 5.2 shows the simulation results of the back-EMF differences and phase currents. From the simulation results, we can see that the zero-crossing points of the back-EMF differences (e_{ab}, e_{bc} and e_{ca}) are same as the commutation instants of the phase currents, so back-EMF differences can be directly used in phase currents' commutation. In this section, a sensorless control method based on the work in [38][39] will be discussed.

As mentioned in Chapter 2, the three terminal voltages of BLDC motor can be shown below:

$$V_{an} = Ri_a + L\frac{\mathrm{d}i_a}{\mathrm{d}t} + e_a \tag{5.8}$$

$$V_{bn} = Ri_b + L\frac{\mathrm{d}i_b}{\mathrm{d}t} + e_b \tag{5.9}$$

$$V_{cn} = Ri_c + L\frac{\mathrm{d}i_c}{\mathrm{d}t} + e_c \tag{5.10}$$

where V_{an}, V_{bn} and V_{cn} are the phase voltages referenced to the motor neutral voltage, R is the phase stator resistance, L is the phase stator inductance, i_a, i_b and i_c are the phase currents, and e_a, e_b and e_c are the phase back-EMFs.

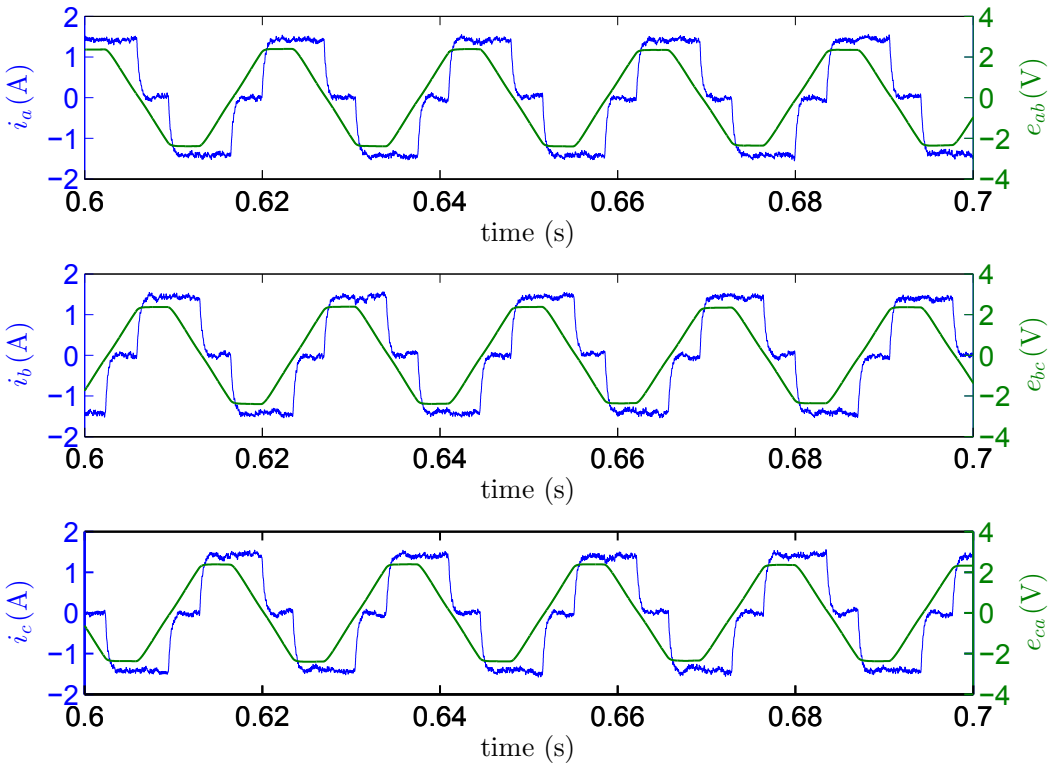

Figure 5.2: Simulations results of the back-EMF differences and phase currents at 700 rpm with 0.04 Nm load

The three line voltages of BLDC motor can be calculated from the terminal voltages as:

$$V_{ab} = R(i_a - i_b) + L\frac{\mathrm{d}(i_a - i_b)}{\mathrm{d}t} + e_a - e_b \tag{5.11}$$

$$V_{bc} = R(i_b - i_c) + L\frac{\mathrm{d}(i_b - i_c)}{\mathrm{d}t} + e_b - e_c \tag{5.12}$$

$$V_{ca} = R(i_c - i_a) + L\frac{\mathrm{d}(i_c - i_a)}{\mathrm{d}t} + e_c - e_a \tag{5.13}$$

where V_{ab}, V_{bc} and V_{ca} are the three line voltages.

Laplace transform results of the line voltages are shown below:

$$V_{ab}(s) = R(i_{ab}(s)) + Ls(i_{ab}(s)) + e_{ab}(s) \tag{5.14}$$

$$V_{bc}(s) = R(i_{bc}(s)) + Ls(i_{bc}(s)) + e_{bc}(s) \tag{5.15}$$

$$V_{ca}(s) = R(i_{ca}(s)) + Ls(i_{ca}(s)) + e_{ca}(s) \tag{5.16}$$

where $V_{ab}(s)$, $V_{bc}(s)$ and $V_{ca}(s)$ are the Laplace transforms of the three line voltages, $e_{ab}(s)$, $e_{bc}(s)$ and $e_{ca}(s)$ are the Laplace transforms of the back-EMF differences and $i_{ab}(s)$, $i_{bc}(s)$ and $i_{ca}(s)$ are the Laplace transforms of the line currents.

For each equation above, we take the line voltage as the inputs, the back-EMF difference as the disturbances and the line current as the outputs, so we can build different models for the three equations.

The disturbance observer structure can be applied to estimate disturbances. As shown in Figure 5.3 [38], The actual plant transfer function is $P'(s)$. $-\hat{e}_{ab}$, $-\hat{e}_{bc}$ and $-\hat{e}_{ca}$ are the estimated back-EMF differences. $P(s)$ is the nominal plant transfer function. The inverse of the nominal plant transfer function is $P^{-1}(s)$. n is the line currents measurement noise which can be filtered out by the low pass filter. $Q(s)$ is the low pass filter transfer function.

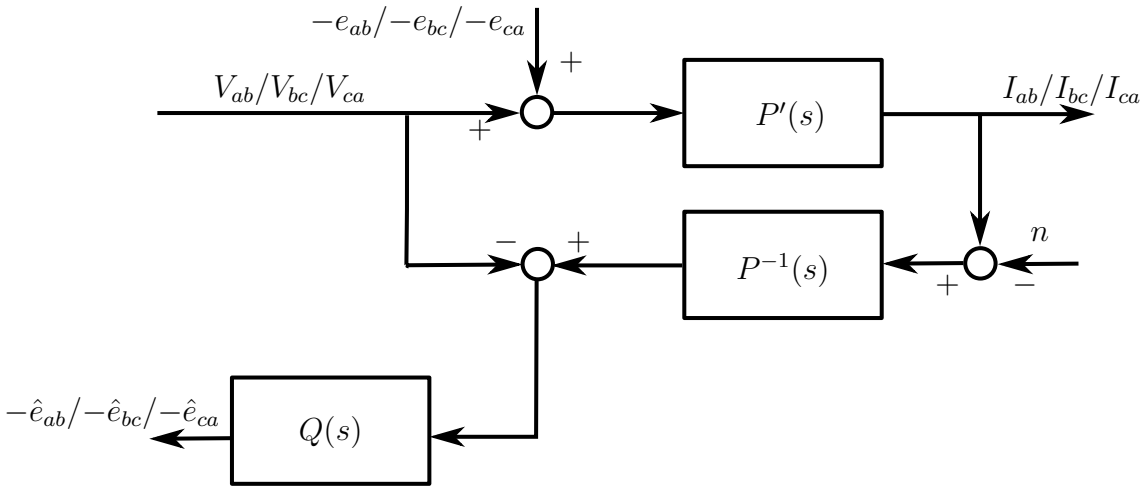

Figure 5.3: Disturbance observer structure based back-EMF differences estimation method

For the estimated disturbances, they are not used to implement disturbance rejection. Instead, estimated disturbances are used as the inputs of the commutation algorithms, and their zero-crossing points will be commutation instants of the BLDC motor.

In commutation states 0 and 3, the zero-crossing points of $\hat{e}_{bc}$ are the

commutation instants of the BLDC motor. In commutation states 1 and 4, the zero-crossing points of $\hat{e}_{ab}$ are the commutation instants of the BLDC motor. In commutation states 2 and 5, the zero-crossing points of $\hat{e}_{ca}$ are the commutation instants of the BLDC motor.

5.3 Design of the Disturbance Observer

For the design of a disturbance observer, the most important part is to design the low pass filter $Q(s)$. $Q(s)$ used in this chapter is designed based on the parameters of the DRV8312 DMC board.

As mentioned in Chapter 4, the terminal voltage of each phase is measured by a voltage resistor divider circuit and a first-order low pass filter. The transfer function of the terminal voltage measurement circuit is:

$$T(s) = \frac{V_{out}}{V_{in}} = \frac{R_2}{R_1 + R_2 + R_1 R_2 C s} \tag{5.17}$$

where R_1 and R_2 are the divider resistances, C is the low pass filter capacitance, V_{in} is the input signal and V_{out} is the filtered waveform of V_{in}.

The relationship between measured line voltages and real line voltages are shown in equations below:

$$\hat{V}_{ab}(s) = T(s) \cdot V_{ab}(s) \tag{5.18}$$

$$\hat{V}_{bc}(s) = T(s) \cdot V_{bc}(s) \tag{5.19}$$

$$\hat{V}_{ca}(s) = T(s) \cdot V_{ca}(s) \tag{5.20}$$

where $\hat{V}_{ab}(s)$, $\hat{V}_{bc}(s)$ and $\hat{V}_{ca}(s)$ are the measured line voltages, $V_{ab}(s)$, $V_{bc}(s)$ and $V_{ca}(s)$ are the Laplace transforms of the three line voltages.

The cutoff frequency f_{cut} of the terminal voltage measurement circuit can be shown below:

$$f_{cut} = \frac{R_1 + R_2}{2\pi R_1 R_2 C} \tag{5.21}$$

With the parameters in Table 4.3, the transfer function and cutoff frequency f_{cut} can be calculated as:

$$T(s) = \frac{V_{out}}{V_{in}} = \frac{223.3}{s + 4487.1} \tag{5.22}$$

$$f_{cut} = 714.2\,\text{Hz} \tag{5.23}$$

The low pass filter $Q(s)$ is designed to be the same as the transfer function of the terminal voltage measurement circuit.

$$Q(s) = T(s) = \frac{223.3}{s + 4487.1} \tag{5.24}$$

For the measurement of three phase currents, three differential amplifier circuits are used to measure three phase currents. The per unit range of -1.0 to 1.0 is corresponding to the real current from $-8.65\,\text{A}$ to $8.65\,\text{A}$. The relationship can be shown in equations below:

$$I_{ab}(s) = K \cdot \hat{I}_{ab} \tag{5.25}$$

$$I_{bc}(s) = K \cdot \hat{I}_{bc} \tag{5.26}$$

$$I_{ca}(s) = K \cdot \hat{I}_{ca} \tag{5.27}$$

$$K = 8.65\,\text{A} \tag{5.28}$$

where $i_{ab}(s)$, $i_{bc}(s)$ and $i_{ca}(s)$ represent line currents. $\hat{I}_{ab}$, $\hat{I}_{bc}$ and $\hat{I}_{ca}$ are per unit line currents.

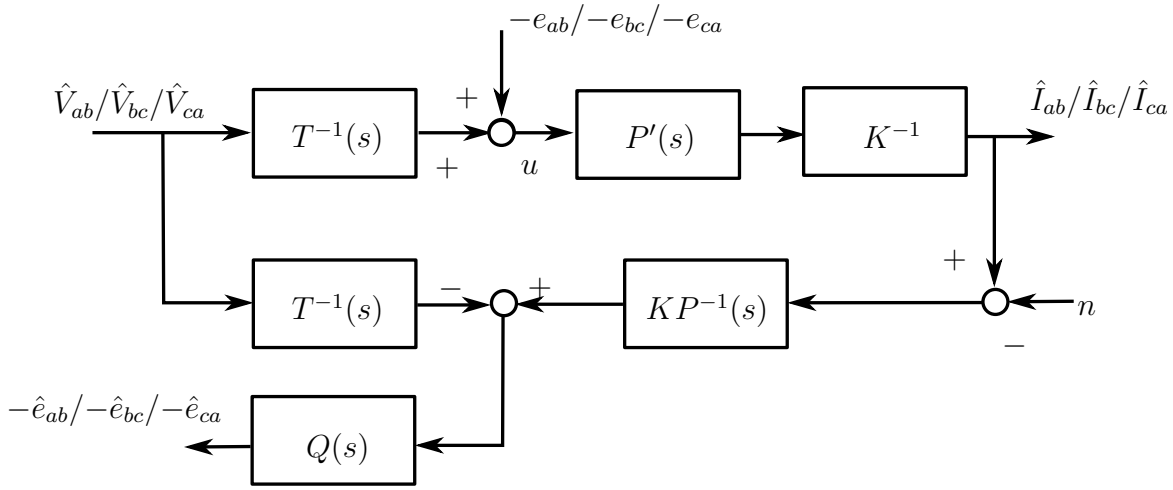

Figure 5.4: Modified disturbance observer structure considering voltage and current sensing circuits

The modified disturbance observer structure is shown in Figure 5.4 [38]. The estimated back-EMF differences $-\hat{e}_{ab}$, $-\hat{e}_{bc}$ and $-\hat{e}_{ca}$ can be shown as

[38]:

$$-\hat{e}_{ab} = -\hat{V}_{ab} \cdot T^{-1}(s) \cdot Q(s) + K \cdot P^{-1}(s) \cdot Q(s) \cdot (\hat{I}_{ab} - n) \tag{5.29}$$

$$-\hat{e}_{bc} = -\hat{V}_{bc} \cdot T^{-1}(s) \cdot Q(s) + K \cdot P^{-1}(s) \cdot Q(s) \cdot (\hat{I}_{bc} - n) \tag{5.30}$$

$$-\hat{e}_{ca} = -\hat{V}_{ca} \cdot T^{-1}(s) \cdot Q(s) + K \cdot P^{-1}(s) \cdot Q(s) \cdot (\hat{I}_{ca} - n) \tag{5.31}$$

The per unit line currents $\hat{I}_{ab}$, $\hat{I}_{bc}$ and $\hat{I}_{ca}$ can be shown as:

$$\hat{I}_{ab} = [\hat{V}_{ab} \cdot T^{-1}(s) - e_{ab}] \cdot P'(s) \cdot K^{-1} \tag{5.32}$$

$$\hat{I}_{bc} = [\hat{V}_{bc} \cdot T^{-1}(s) - e_{bc}] \cdot P'(s) \cdot K^{-1} \tag{5.33}$$

$$\hat{I}_{ca} = [\hat{V}_{ca} \cdot T^{-1}(s) - e_{ca}] \cdot P'(s) \cdot K^{-1} \tag{5.34}$$

Then $-\hat{e}_{ab}$, $-\hat{e}_{bc}$ and $-\hat{e}_{ca}$ can be modified as [38]:

$$\begin{aligned} -\hat{e}_{ab} = &-\hat{V}_{ab} \cdot T^{-1}(s) \cdot Q(s) + P^{-1}(s) \cdot P'(s) \cdot \hat{V}_{ab} \cdot T^{-1}(s) \cdot Q(s) \\ &+ [-P^{-1}(s) \cdot P'(s) \cdot e_{ab} - nKP^{-1}(s)] \cdot Q(s) \end{aligned} \tag{5.35}$$

$$\begin{aligned} -\hat{e}_{bc} = &-\hat{V}_{bc} \cdot T^{-1}(s) \cdot Q(s) + P^{-1}(s) \cdot P'(s) \cdot \hat{V}_{bc} \cdot T^{-1}(s) \cdot Q(s) \\ &+ [-P^{-1}(s) \cdot P'(s) \cdot e_{bc} - nKP^{-1}(s)] \cdot Q(s) \end{aligned} \tag{5.36}$$

$$\begin{aligned} -\hat{e}_{ca} = &-\hat{V}_{ca} \cdot T^{-1}(s) \cdot Q(s) + P^{-1}(s) \cdot P'(s) \cdot \hat{V}_{ca} \cdot T^{-1}(s) \cdot Q(s) \\ &+ [-P^{-1}(s) \cdot P'(s) \cdot e_{ca} - nKP^{-1}(s)] \cdot Q(s) \end{aligned} \tag{5.37}$$

If there is no modeling error, $P'(s)$ and $P(s)$ are equal as:

$$P'(s) = P(s) = \frac{1}{Ls + R} \tag{5.38}$$

where R is the phase stator resistance and L is the phase stator inductance.

The low pass filter can filter out the measurement noise n. Then, $-\hat{e}_{ab}$, $-\hat{e}_{bc}$ and $-\hat{e}_{ca}$ can be simplified as [38]:

$$-\hat{e}_{ab} = -e_{ab} \cdot Q(s) \tag{5.39}$$

$$-\hat{e}_{bc} = -e_{bc} \cdot Q(s) \tag{5.40}$$

$$-\hat{e}_{ca} = -e_{ca} \cdot Q(s) \tag{5.41}$$

Thus, the modified disturbance observer structure can be applied to estimate the back-EMF differences:

$$\begin{aligned}\hat{e}_{ab} &= \hat{V}_{ab} - K \cdot P^{-1}(s) \cdot Q(s) \cdot \hat{I}_{ab} \\ \hat{e}_{bc} &= \hat{V}_{bc} - K \cdot P^{-1}(s) \cdot Q(s) \cdot \hat{I}_{bc} \\ \hat{e}_{ca} &= \hat{V}_{ca} - K \cdot P^{-1}(s) \cdot Q(s) \cdot \hat{I}_{ca}\end{aligned} \tag{5.42}$$

5.4 Phase Delay Compensation

Although the sensorless control method based on the disturbance observer does not require a 30 electrical degree shift, phase delay will be introduced because of low pass filters applied in the designed disturbance observer structure. Figure 5.5 shows the waveforms of the real back-EMF differences and the estimated back-EMF differences at a speed of 1000 r/min. From the simulation results, we can see that the estimated back-EMF differences lag the real back-EMF differences. Figure 5.6 shows the condition at a speed of 2000 r/min. Compared with Figure 5.5, we can see that the phase delay becomes larger at a higher speed.

Ideally, the zero-crossing points of back-EMF differences can be treated as the commutation instants of a BLDC motor. But due to the phase delay introduced by low pass filters, phase delay compensation should be done to ensure the correct commutation instants.

Based on the BLDC motor electrical period, the phase delay introduced by low pass filters can be calculated as:

$$\begin{aligned}\theta &= \tan^{-1}\left(\frac{R_1 \cdot R_2 \cdot C \cdot \omega_e}{R_1 + R_2}\right) \\ &= \tan^{-1}\left(\frac{R_1 \cdot R_2 \cdot C}{R_1 + R_2} \cdot \frac{2\pi}{T}\right)\end{aligned} \tag{5.43}$$

where θ is the phase delay, T is one electrical period, R_1 and R_2 are the divider resistances and C is the low pass filter capacitance.

For each of the six commutation states, one back-EMF difference is chosen to identify the commutation instant. The back-EMF difference will start from a maximum positive value or a minimum negative value, then it will reach the

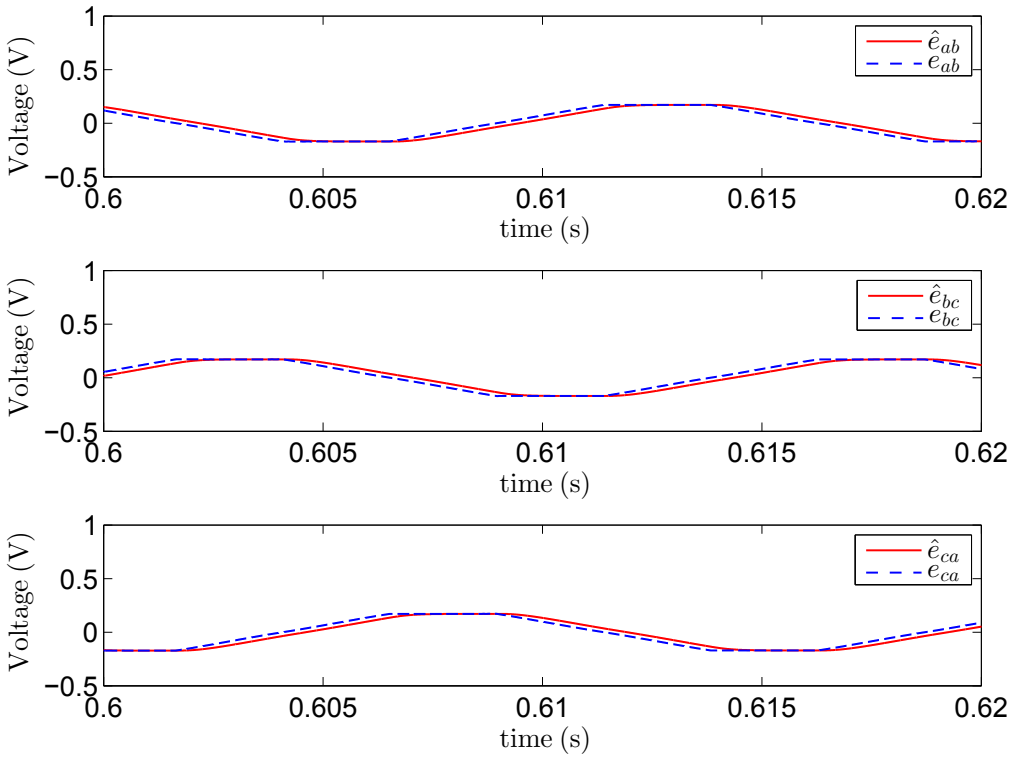

Figure 5.5: Simulation results of the estimated back-EMF differences and the real back-EMF differences at 1000 rpm with 0.04 Nm load

zero-crossing point. Theoretically, the back-EMF difference shape is trapezoidal, so we can assume that each chosen back-EMF difference varies linearly with electrical angle during its commutation state.

To compensate the phase delay, threshold values ,which trigger commutation instants, should be set based on the calculated phase delay instead of zero [38]. With the similar triangles formula, the threshold values used in the chapter to compensate the phase delay can be calculated as [38]:

$$V_p = \frac{\theta}{60^\circ} \cdot V_{pmax} \tag{5.44}$$

$$V_n = \frac{\theta}{60^\circ} \cdot V_{pmin} \tag{5.45}$$

where V_p is the threshold value when the back-EMF difference varies from the maximum positive value to zero, V_n is the threshold value when the back-EMF difference varies from the minimum negative value to zero, θ is the calculated

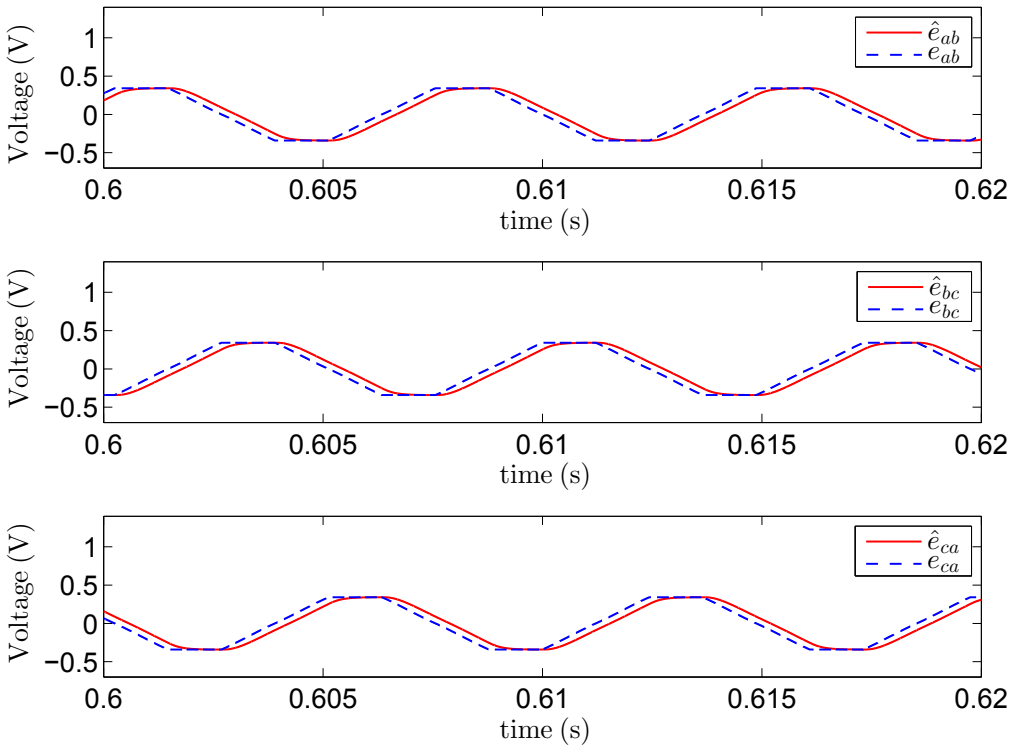

Figure 5.6: Simulation results of the estimated back-EMF differences and the real back-EMF differences at 2000 rpm with 0.04 Nm load

phase delay, V_{pmax} is the maximum positive value of the back-EMF difference and V_{pmin} is the minimum negative value of the back-EMF difference.

Figure 5.7 shows the software flowchart of the sensorless commutation method based on the disturbance observer. At the beginning of commutation states 0, 2 and 4, the estimated value of the chosen back-EMF difference is regarded as the minimum negative value V_{pmin}. At the beginning of commutation states 1, 3 and 5, the estimated value of the chosen back-EMF difference is regarded as the maximum positive value V_{pmax}. Also, the phase delay θ is calculated at this point based on the motor speed. Then the threshold values (V_p and V_n) can be calculated based on the equations above.

In order to minimize the influence of noises, a counter is applied to calculate how many times the estimated back-EMF difference value crosses the threshold value. When the counter reaches a predefined value T_{noises}, this point is treated as the commutation instant and the BLDC motor will switch to the next state.

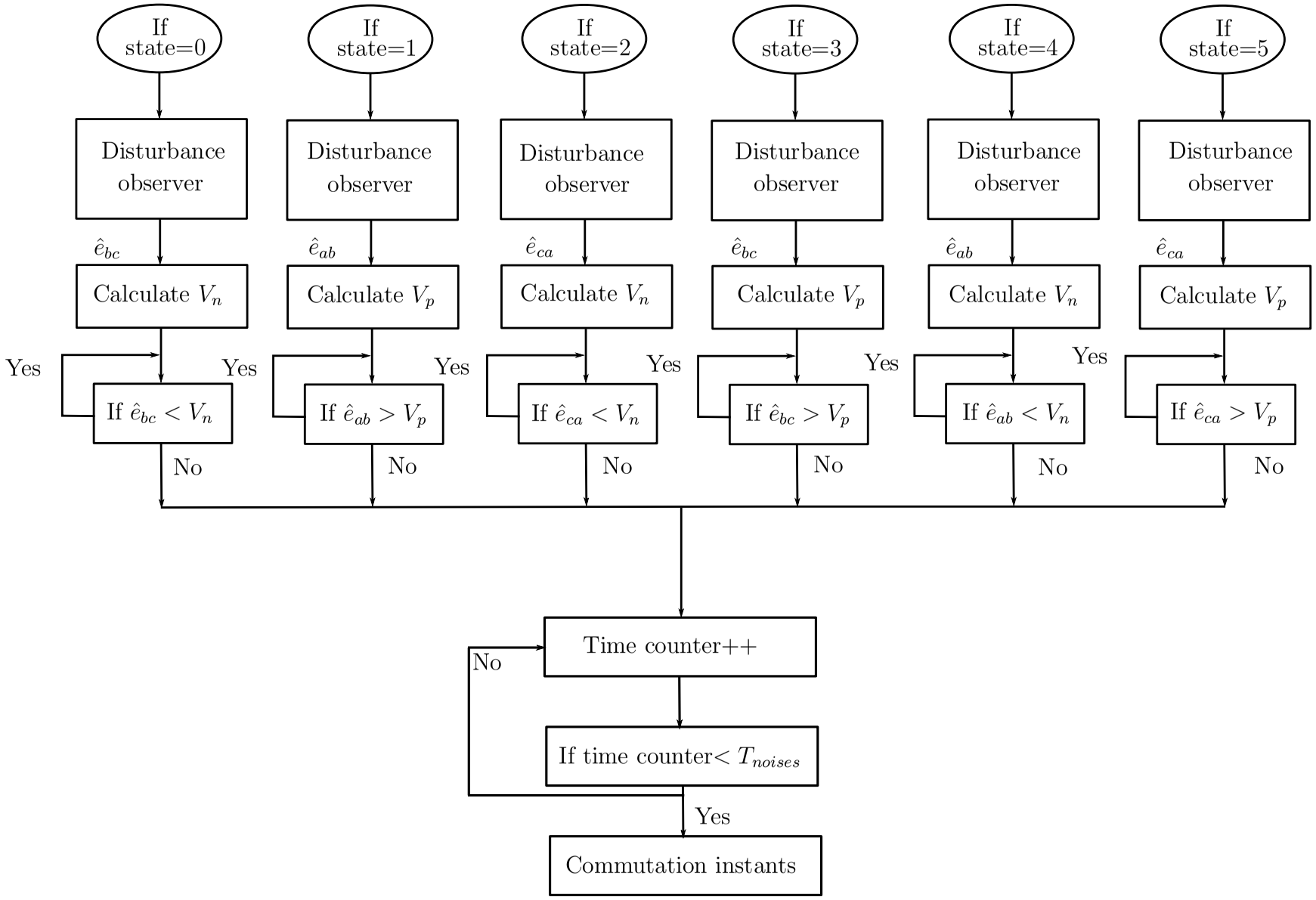

Figure 5.7: Software flowchart of the sensorless commutation method based on the disturbance observer structure

5.5 Proposed Sensorless Drive

Figure 5.8 shows the proposed sensorless drive for speed control of a BLDC motor. A proportional integral (PI) controller is applied to determine the duty cycle of the PWM signals based on the difference between the measured motor speed ω and the reference motor speed ω^*.

The measured three phase currents and the three phase terminal voltages are the inputs of the disturbance observer. The estimated back-EMF differences $\hat{e}_{ab}$, $\hat{e}_{bc}$ and $\hat{e}_{ca}$ together with the measured motor speed are the inputs of the commutation trigger block. The commutation sequence of the proposed method is shown in Table 5.1.

Because the proposed method is based on back-EMF differences, a starting procedure is required to speed up the BLDC motor to a higher speed. In this chapter, the conventional open-loop starting method, as described in Chapter 4, is applied to blindly start the BLDC motor.

Commutation States	Commutation Instants
0	$\hat{e}_{bc} = V_n$
1	$\hat{e}_{ab} = V_p$
2	$\hat{e}_{ca} = V_n$
3	$\hat{e}_{bc} = V_p$
4	$\hat{e}_{ab} = V_n$
5	$\hat{e}_{ca} = V_p$

Table 5.1: Commutation sequence for the method based on disturbance observer

5.6 Experimental Results

In this section, we present the experiment results of the proposed sensorless BLDC motor drive based on the disturbance observer structure at different speeds. Compensation of the phase delay introduced by the disturbance observer structure is also discussed.

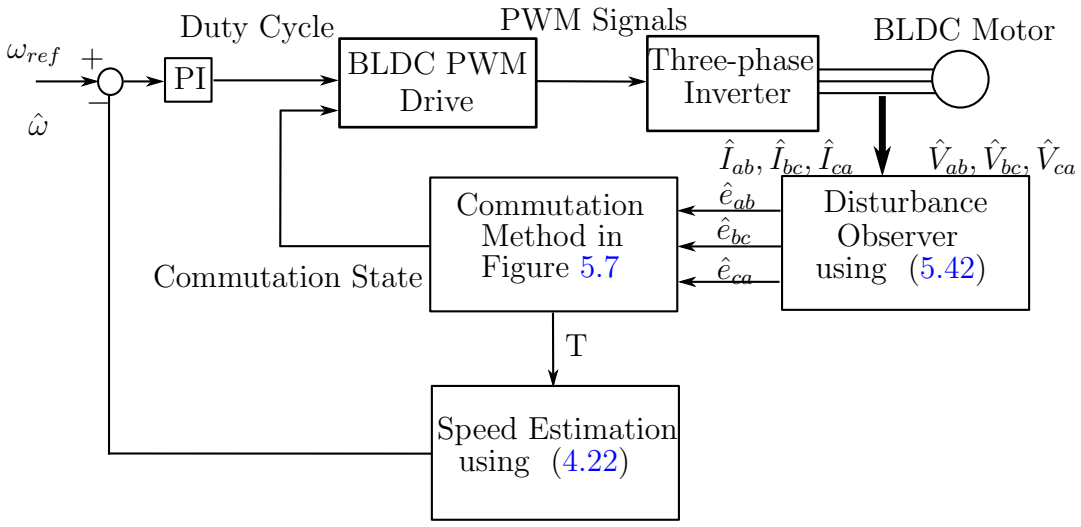

Figure 5.8: Proposed sensorless BLDC motor drive based on the disturbance observer structure

5.6.1 Experiment Results at 600 rpm

Figure 5.9 shows the estimated back-EMF differences at 600 rpm. Figure 5.10 shows the speed response at 600 rpm.

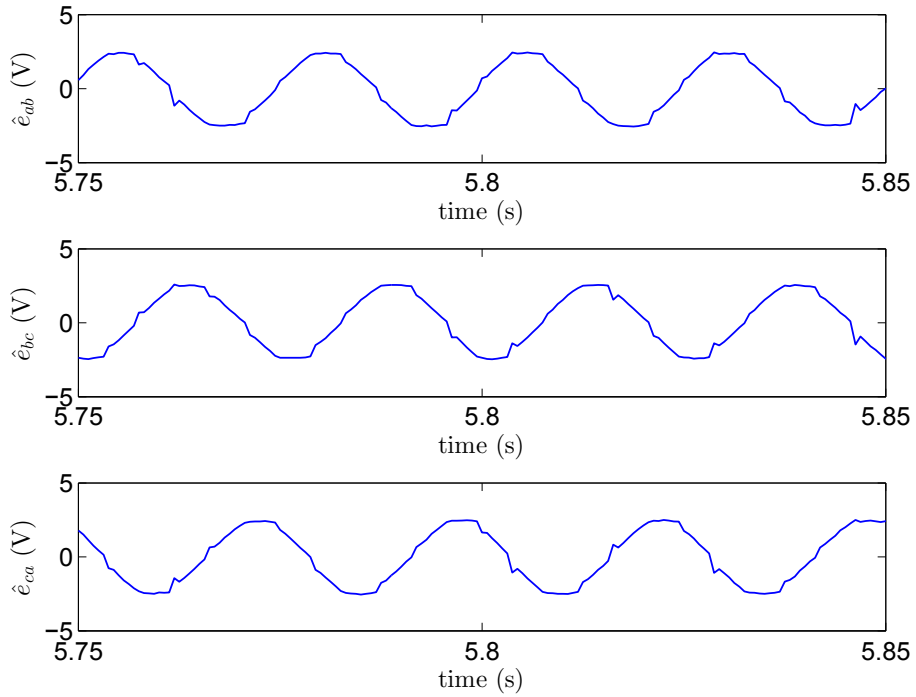

Figure 5.9: Experiment results of estimated back-EMF differences at 600 rpm

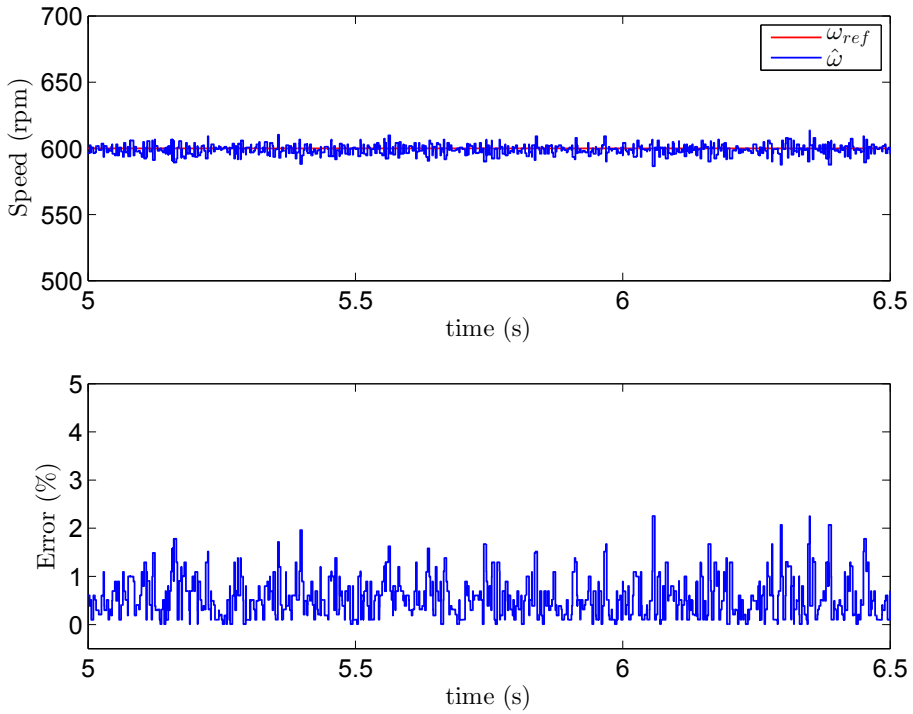

Figure 5.10: Speed response at 600 rpm

5.6.2 Experiment Results at 1000 rpm

Figure 5.11 shows the estimated back-EMF differences at 1000 rpm. Figure 5.12 shows the speed response at 1000 rpm.

Based on the results in subsection 5.6.1 and subsection 5.6.2, we can see that the estimated back-EMF differences waveforms are symmetric, and the speed of the BLDC motor can remain stable with negligible error.

5.6.3 Phase Delay Compensation

In this section, we present the experiment results at 1500 rpm to verify the effectiveness of the phase compensation method introduced in section 5.4.

Figure 5.13 shows the relationship between phase A current i_a and $\hat{e}_{ab}$. We can see that the commutation points of i_a are same with the zero-crossing points of $\hat{e}_{ab}$. Figure 5.14 shows the speed response at 1500 rpm.

Without phase compensation, the BLDC motor stalls sometimes when it runs at 1500 rpm due to inaccurate commutation. Figure 5.15 shows the

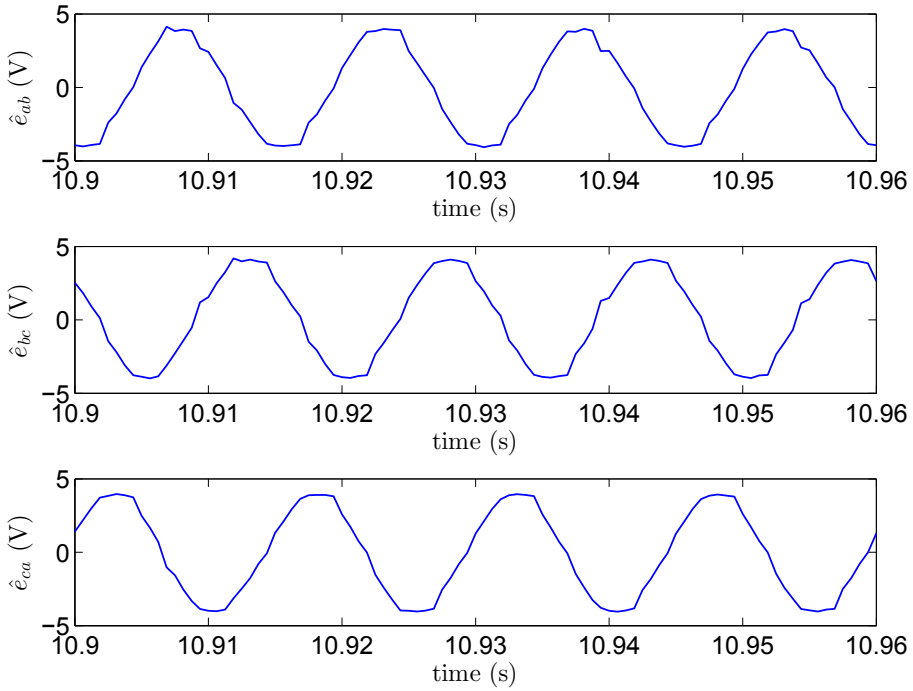

Figure 5.11: Experiment results of estimated back-EMF differences at 1000 rpm

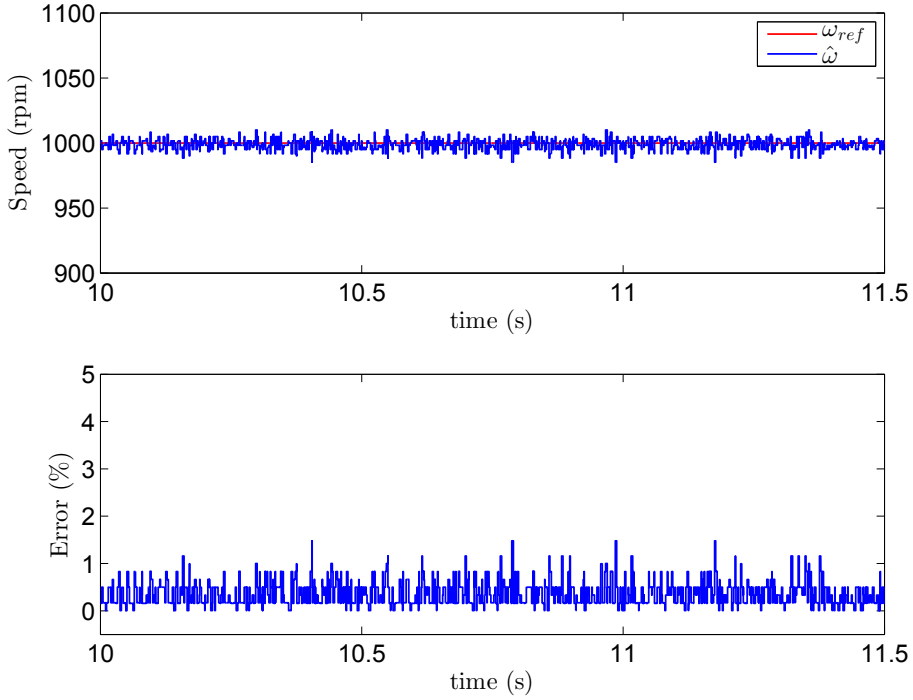

Figure 5.12: Speed response at 1000 rpm

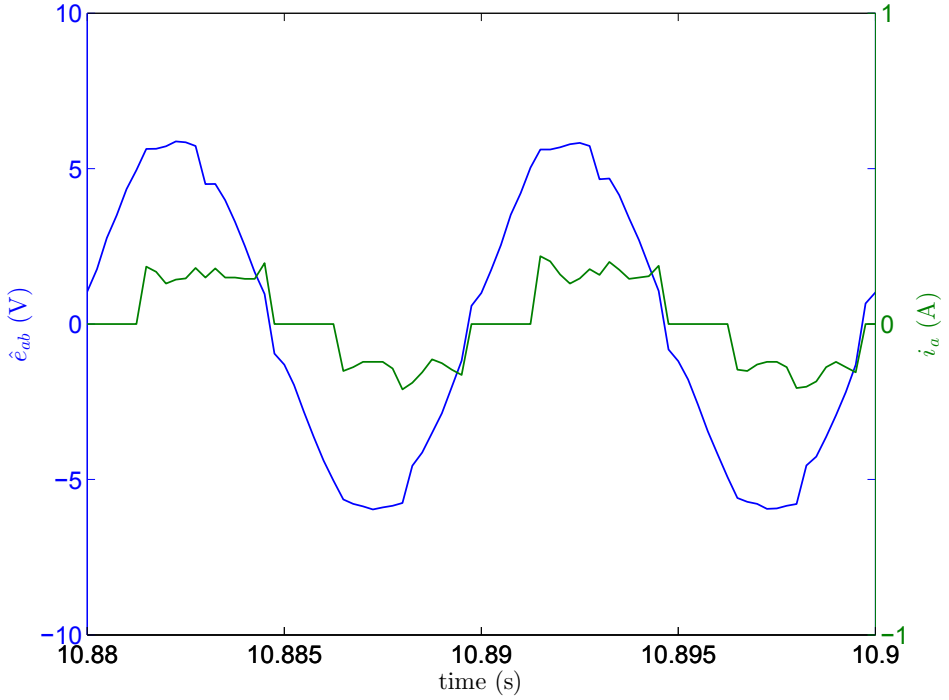

Figure 5.13: Phase A current and $\hat{e}_{ab}$ at 1500 rpm

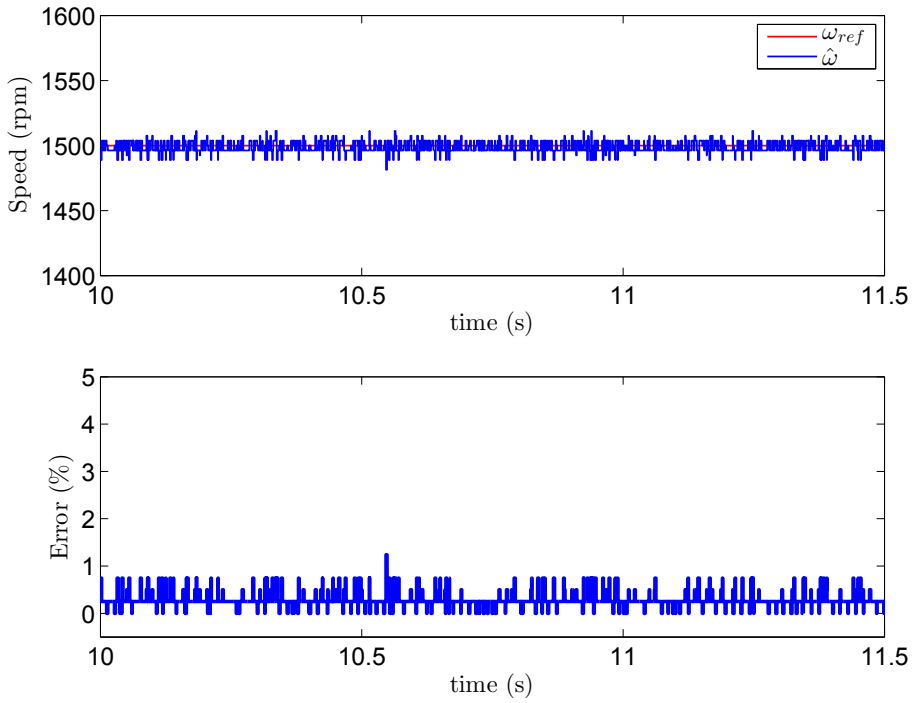

Figure 5.14: Speed response at 1500 rpm

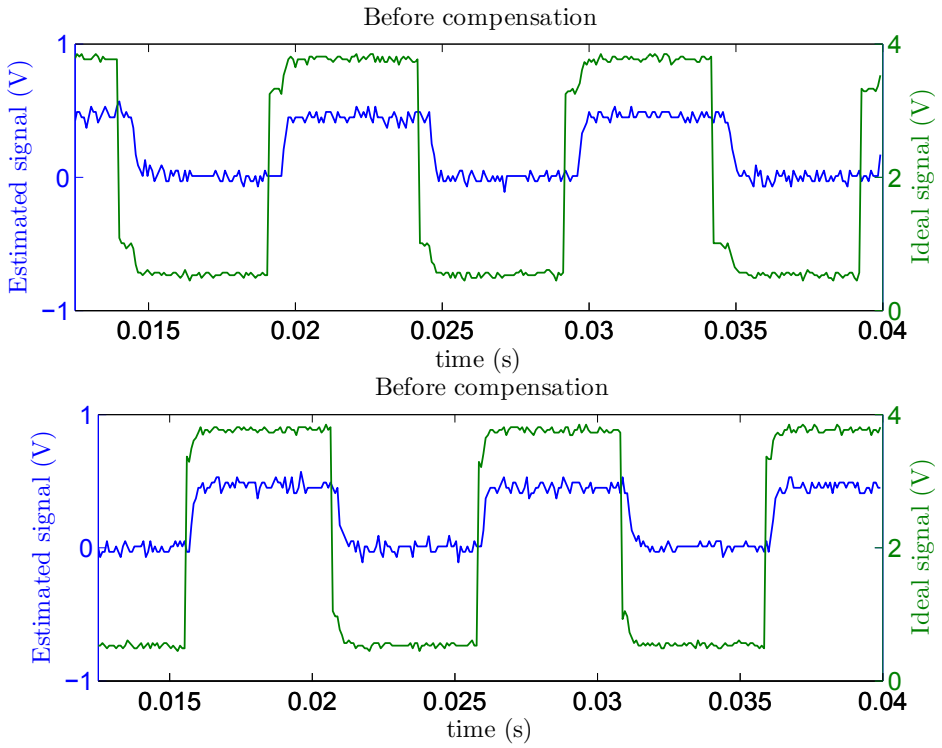

Figure 5.15: Ideal commutation signal and estimated commutation signal at 1500 rpm

experiment results of the relationship between the ideal commutation signal (Hall-effect sensor A output) and the estimated commutation signal (virtual Hall-effect sensor A output obtained from the sensorless commutation method) at 1500 rpm.

From Figure 5.15, we can see that the estimated commutation signal matches well with the ideal commutation signal with phase compensation. For high speed applications, it is necessary to compensate the phase delay caused by the disturbance observer structure [38].

With phase compensation method, the sensorless commutation method can get accurate commutation points, and the high speed range can be expanded.

5.7 Comparison with the Sensorless Drive based on Line Voltage Differences

In this section, we make a comparison of the proposed sensorless BLDC motor drive based on the disturbance observer structure and the sensorless drive introduced in Chapter 4.

Based on the analysis above, both of these two sensorless drives can achieve precise sensorless commutation. However, they all need compensation for the phase delay caused by the low pass filter. The electrical frequency of the motor must be smaller than the cutoff frequency f_{cut} of the low pass filter, which is 714.2 Hz.

For the sensorless drive based on the line voltage differences, the maximum allowable phase delay from the low pass filter is 30° (electrical frequency equals 412.5 Hz). In contrast, the maximum allowable phase delay is 60° (electrical frequency equals 1237.4 Hz) for the sensorless BLDC motor drive based on the disturbance observer structure. For the given motor drive board, we can see that disturbance observer based sensorless drive allows the electrical frequency of the motor to be up to the cutoff frequency of the low pass filter. Disturbance observer based sensorless drive has a wider high speed range in comparison with the sensorless drive based on the line voltage differences.

Both of these two sensorless drives are based on back-EMFs, so they all have poor performance in the low speed range. Figure 5.16 shows V_{abca} and $\hat{e}_{ab}$ waveforms at low speeds. We can see that the waveforms are distorted, and we can not get accurate commutation points with either of the proposed sensorless drives.

Figure 5.17 and Figure 5.18 show the simulation results of the speed response at low speed (500 rpm) and high speed (1500 rpm) during loading transient, respectively. For 500 rpm, a step load (0.05 Nm) is applied at 0.3 s. For 1500 rpm, a step load (0.05 Nm) is applied at 0.5 s. From the simulation results, we can see that the speed response of the two sensorless drives are similar. For both low and high speeds conditions, the motor speed decreases after applying the load, and then it will keep on tracking the reference speed

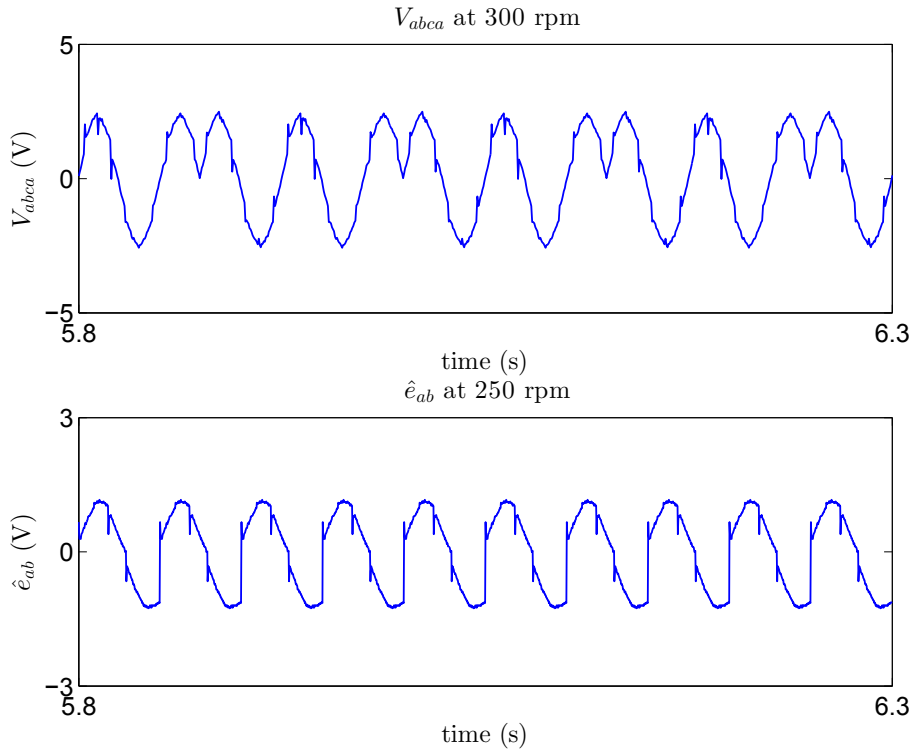

Figure 5.16: V_{abca} at 300 rpm and $\hat{e}_{ab}$ at 250 rpm

after the transient time.

5.8 Summary

In this chapter, we discuss a sensorless commutation method based on the disturbance observer. The sensorless commutation method with is implemented in the experimental environment, and it works well at different speeds. Compared with sensorless commutation method based on line voltage differences, disturbance observer based method has a wider high speed range, and it does not require a 30° phase shift to get the correct commutation points.

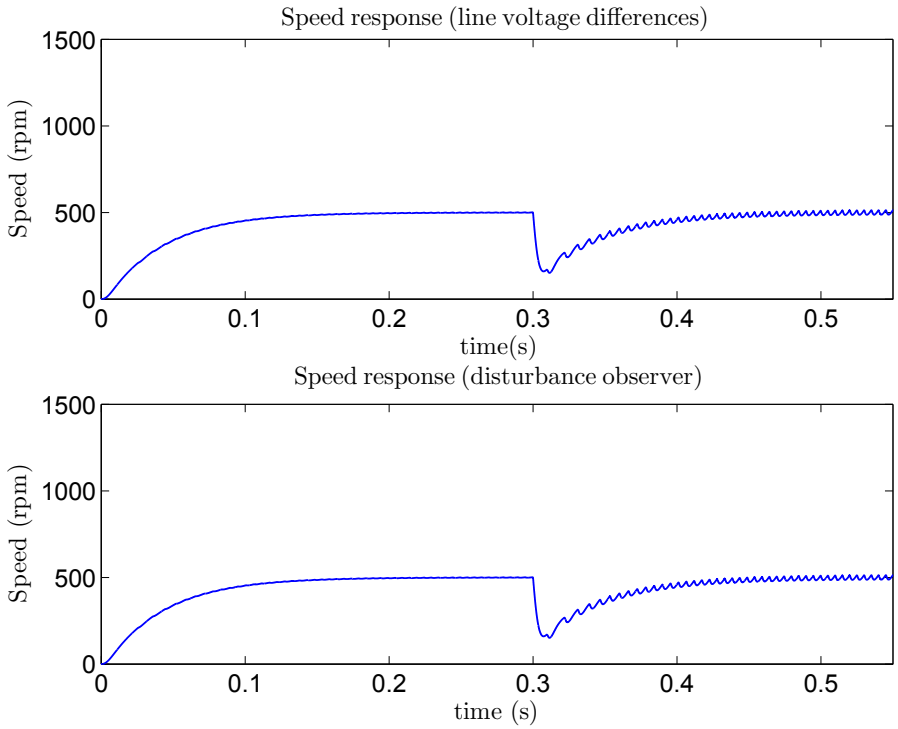

Figure 5.17: Speed response at 500 rpm during loading transient

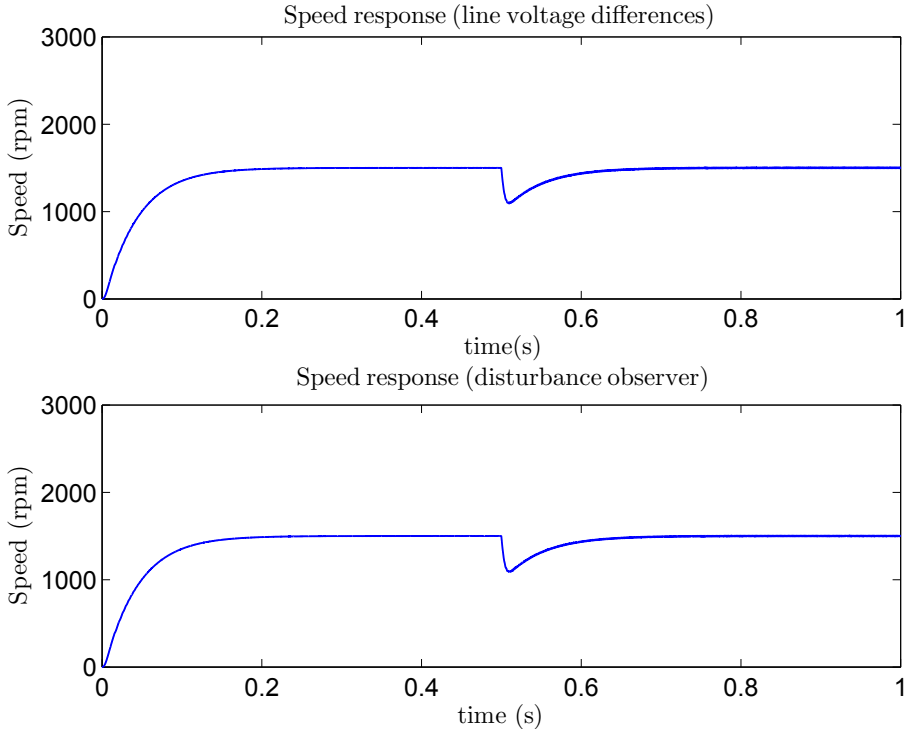

Figure 5.18: Speed response at 1500 rpm during loading transient

Chapter 6

Conclusions

6.1 Summary of Research

This thesis focuses on the implementation of two sensorless control techniques for a BLDC motor. Firstly, we discuss a sensorless control method, which utilizes line voltage differences to estimate the zero-crossing points of back-EMFs. The line voltage differences have the same zero-crossing points as back-EMFs, which are verified by the simulation results. This method only requires three motor terminal voltages without the need for the motor neutral voltage. This sensorless control method is also implemented in the experimental environment, and a compensation method is applied to compensate the phase delay introduced by the the low-pass filters in the terminal voltage sensing circuits.

Then we introduce a back-EMF differences based sensorless control method, which does not require any phase shift to get the commutation instants. The disturbance observer structure is applied to estimate the back-EMF differences. Simulation results show that the estimated back-EMF differences matches well with the real back-EMF differences except for a phase delay caused by the low pass filter in the disturbance observer structure. This sensorless control method with phase delay compensation is implemented in the experimental environment.

From the experiment results, we conclude that both of these two sensorless control techniques can be applied in commutating a BLDC motor. Phase delay compensation methods are necessary for high speed operation. Disturbance observer based method has a better high speed capability. Because both of

these two sensorless control techniques are based on back-EMFs, they have limiting low speed capability. Based on the Simulink simulation results, both of these two sensorless drives are able to work well even with load disturbance.

6.2 Future Work

In the past few decades, fuzzy logic controllers gained wide attentions and have been applied in BLDC motor drives [32][34]. Fuzzy controller-based BLDC motor drive has a better performance for the varying operating conditions of the motor, such as motor parameters variation and load uncertainties [34]. For the future work, we will apply the fuzzy logic controller in the speed control loop, together with the sensorless commutation techniques investigated in this thesis, to build a combined BLDC sensorless control drive with better performance.

Bibliography

[1] R. Becerra, T. Jahns, and M. Ehsani. Four-quadrant sensorless brushless ecm drive. In *Applied Power Electronics Conference and Exposition, 1991. APEC'91. Conference Proceedings, 1991., Sixth Annual*, pages 202–209. IEEE, 1991.

[2] M. Bonfe and M. Bergo. A brushless motor drive with sensorless control for commercial vehicle hydraulic pumps. In *2008 IEEE International Symposium on Industrial Electronics*, pages 612–617. IEEE, 2008.

[3] C. W. Brokish. Emulation fundamentals for tis dsp solutions. *Texas Instruments Application Report SPRA439C*, 2005.

[4] C.-H. Chen and M.-Y. Cheng. A new sensorless commutation drive for brushless dc motors and alternators. In *2006 IEEE International Symposium on Industrial Electronics*, volume 3, pages 2116–2121. IEEE, 2006.

[5] W.-H. Chen, J. Yang, L. Guo, and S. Li. Disturbance-observer-based control and related methodsan overview. *IEEE Transactions on Industrial Electronics*, 63(2):1083–1095, 2016.

[6] P. Damodharan and K. Vasudevan. Sensorless brushless dc motor drive based on the zero-crossing detection of back electromotive force (emf) from the line voltage difference. *IEEE Transactions on Energy Conversion*, 25(3):661–668, 2010.

[7] A. Deenadayalan, C. Dhananjai, and G. S. Ilango. Modified sliding mode observer for wide speed range operation of brushless dc motor. *Frontiers of Electrical and Electronic Engineering*, 7(4):467–476, 2012.

[8] J. C. Gamazo-Real, E. Vázquez-Sánchez, and J. Gómez-Gil. Position and speed control of brushless dc motors using sensorless techniques and application trends. *Sensors*, 10(7):6901–6947, 2010.

[9] A. Girolkar and G. Bhuvaneswari. Control of pmbldc motor using third harmonic back emf sensing with zigzag transformer. In *Electrical Energy Systems (ICEES), 2014 IEEE 2nd International Conference on*, pages 110–115. IEEE, 2014.

[10] D. C. Hanselman. *Brushless permanent magnet motor design*. The Writers' Collective, 2003.

[11] F. Hicham, D. Mohamed, R. Abdellatif, and B. Pierre. Sliding mode observer for position and speed estimations in brushless dc motor (bldcm). In *Industrial Technology, 2004. IEEE ICIT'04. 2004 IEEE International Conference on*, volume 1, pages 121–126. IEEE, 2004.

[12] T. Hurd and I. Sever. Hardware-controlled brushless dc motors ease the burden on cpus. *EDN (Electrical Design News)*, 55(16):24, 2010.

[13] K. Iizuka, H. Uzuhashi, M. Kano, T. Endo, and K. Mohri. Microcomputer control for sensorless brushless motor. *IEEE Transactions on Industry Applications*, (3):595–601, 1985.

[14] M. Ikhlas. *Rotor Position Identification for Brushless DC motor*. PhD thesis, The University of Western Ontario, 2015.

[15] T. Instruments. Drv83x2 three-phase pwm motor driver, december 2014. *URL http://www. ti. com/lit/ds/symlink/drv8332. pdf. Rev: SLES256E–May*, 2010.

[16] T. Instruments. Drv8312-c2-kit hardware reference guide. *C2000 & DRV8312 Systems and Applications Team, Apr*, 2011.

[17] T. Instruments. Tms320x2802x, 2803x piccolo analog to digital converter (adc) and comparator. *Reference Guide, Dec*, 2011.

[18] T. Instruments. Tms320x2802x, 2803x piccolo enhanced pulse width modulator (epwm) module. *Reference Guide, Mar*, 2011.

[19] T. Kim, C. Kim, and J. Lyou. A new sensorless drive scheme for a bldc motor based on the terminal voltage difference. In *IECON 2011-37th Annual Conference on IEEE Industrial Electronics Society*, pages 1710–1715. IEEE, 2011.

[20] T. Kim, H. Lee, and M. Ehsani. Position sensorless brushless dc motor/generator drives: review and future trends. *IET Electric Power Applications*, 1(4):557–564, 2007.

[21] T.-H. Kim, H.-W. Lee, and M. Ehsani. State of the art and future trends in position sensorless brushless dc motor/generator drives. In *31st Annual Conference of IEEE Industrial Electronics Society, 2005. IECON 2005.*, pages 8–pp. IEEE, 2005.

[22] T.-S. Kim, B.-G. Park, D.-M. Lee, J.-S. Ryu, and D.-S. Hyun. A new approach to sensorless control method for brushless dc motors. *International Journal of Control, Automation, and Systems*, 6(4):477–487, 2008.

[23] R. Krishnan. *Permanent magnet synchronous and brushless DC motor drives*. CRC press, 2009.

[24] Y.-S. Lai and Y.-K. Lin. Novel back-emf detection technique of brushless dc motor drives for wide range control without using current and position sensors. *IEEE Transactions on power electronics*, 23(2):934–940, 2008.

[25] Y.-S. Lai, F.-S. Shyu, and Y.-H. Chang. Novel loss reduction pulsewidth modulation technique for brushless dc motor drives fed by mosfet inverter. *IEEE transactions on power electronics*, 19(6):1646–1652, 2004.

[26] Z. Li, S. Cheng, Y. Qin, and K. Cai. A novel line-to-line back emf calculation for sensorless brushless dc motor drives. In *Electrical Machines and Systems, 2008. ICEMS 2008. International Conference on*, pages 1406–1411. IEEE, 2008.

[27] P. Madaan. Brushless dc motors–part i: Construction and operating principles. *Cypress Semiconductor*, 11, 2013.

[28] L. Mingyao, Z. Zhiyao, and L. Keman. A novel and easy-realizing initial rotor position detection method and speedup algorithm for sensorless bldc motor drives. *ICEMS 2008*, pages 2860–2865, 2008.

[29] J. C. Moreira. Indirect sensing for rotor flux position of permanent magnet ac motors operating over a wide speed range. *IEEE Transactions on Industry Applications*, 32(6):1394–1401, 1996.

[30] M. Mubeen. Brushless dc motor primer. *Motion Tech Trends*, 2008.

[31] S. Ogasawara and H. Akagi. An approach to position sensorless drive for brushless dc motors. *IEEE Transactions on Industry Applications*, 27(5):928–933, 1991.

[32] A. Rubaai, D. Ricketts, and M. D. Kankam. Laboratory implementation of a microprocessor-based fuzzy logic tracking controller for motion controls and drives. *IEEE Transactions on Industry Applications*, 38(2):448–456, 2002.

[33] E. Schrijver and J. Van Dijk. Disturbance observers for rigid mechanical systems: equivalence, stability, and design. *Journal of Dynamic Systems, Measurement, and Control*, 124(4):539–548, 2002.

[34] R. Shanmugasundram, K. M. Zakariah, and N. Yadaiah. Implementation and performance analysis of digital controllers for brushless dc motor drives. *IEEE/ASME transactions on mechatronics*, 19(1):213–224, 2014.

[35] J. Shao. An improved microcontroller-based sensorless brushless dc (bldc) motor drive for automotive applications. *IEEE Transactions on industry applications*, 42(5):1216–1221, 2006.

[36] J. Shao, D. Nolan, and T. Hopkins. A novel direct back emf detection for sensorless brushless dc (bldc) motor drives. In *Applied Power Electronics*

Conference and Exposition, 2002. APEC 2002. Seventeenth Annual IEEE, volume 1, pages 33–37. IEEE, 2002.

[37] B. Terzic and M. Jadric. Design and implementation of the extended kalman filter for the speed and rotor position estimation of brushless dc motor. *IEEE Transactions on Industrial Electronics*, 48(6):1065–1073, 2001.

[38] S. Wang and A.-C. Lee. A 12-step sensorless drive for brushless dc motors based on back-emf differences. *IEEE Transactions on Energy Conversion*, 30(2):646–654, 2015.

[39] S. Wang, C.-H. Lu, and A.-C. Lee. Disturbance observer structure applied to sensorless brushless dc motors drive. *International Journal of Computer Theory and Engineering*, 7(2):92, 2015.

[40] P. Yedamale. Brushless dc (bldc) motor fundamentals. *Microchip Technology Inc*, 20:3–15, 2003.